Multiphysics simulation of electric motors with an application to stators

N. Hanappier, Eric Charkaluk, N. Triantafyllidis

▶ **To cite this version:**

N. Hanappier, Eric Charkaluk, N. Triantafyllidis. Multiphysics simulation of electric motors with an application to stators. International Journal of Solids and Structures, 2022, 253, pp.111406. 10.1016/j.ijsolstr.2021.111406 . hal-04321641

HAL Id: hal-04321641
https://hal.science/hal-04321641

Submitted on 4 Dec 2023

HAL is a multi-disciplinary open access archive for the deposit and dissemination of scientific research documents, whether they are published or not. The documents may come from teaching and research institutions in France or abroad, or from public or private research centers.

L'archive ouverte pluridisciplinaire **HAL**, est destinée au dépôt et à la diffusion de documents scientifiques de niveau recherche, publiés ou non, émanant des établissements d'enseignement et de recherche français ou étrangers, des laboratoires publics ou privés.

Multiphysics simulation of electric motors with an application to stators

N. Hanappier[a], E. Charkaluk[a,b], N. Triantafyllidis[a,b,c,*]

[a] *Laboratoire de Mécanique des Solides (CNRS UMR 7649), Ecole Polytechnique, Institut Polytechnique de Paris*
[b] *Département de Mécanique, École Polytechnique, Route de Saclay, Palaiseau 91128, FRANCE*
[c] *Aerospace Engineering Department & Mechanical Engineering Department (emeritus), The University of Michigan, Ann Arbor, MI 48109-2140, USA*

Abstract

The development of a new generation of more efficient electric motors leads to designs with higher stresses, currents and electromagnetic fields. To improve on the prevailing existing methodology for the concurrent calculation of electromagnetic and mechanical fields in electric motors, the authors recently presented in Hanappier et al. (2021a) a multiphysics formulation of the problem using the direct (current configuration) approach of continuum mechanics together with analytical solutions of idealized motor problems.

However, due to the complex geometry of a typical electric motor and the nonlinearity of the coupled (magneto-mechanical) constitutive laws, numerical solutions of the governing equations are required. To this end, a Lagrangian (reference configuration) variational principle is proposed for the eddy current approximation that properly retrieves the Maxwell stresses and is consistent with its direct approach counterpart.

Based on this variational principle, a numerical (FEM) approach is proposed. It is next applied to an idealized (cylindrical) stator, where an analytical solution can be found for the linear magnetization regime, thus providing firstly an independent code verification and then an assessment of the influence of the stator's nonlinear magnetic response. The approach is subsequently used to tackle a realistic geometry stator with two pole pairs under a three-phase current for two different cases: loosely or tightly packed conducting wires to calculate the corresponding magnetic, stress and strain fields.

Keywords: Continuum mechanics, Coupled mechanical and electromagnetic processes, Magnetoelasticity, Electric motors, Variational principle, Finite elements

*Corresponding author: nicolas.triantafyllidis@polytechnique.edu

Contents

1. Introduction

The increasing importance of environmental constraints in the transportation industry and the quest to reduce its carbon footprint, leads the electric motor industry to develop higher performance products with reduced manufacturing costs. New goals are set by various entities (López et al., 2019) in terms of efficiency, reliability, power losses, power density, higher rotation velocity and reduced weight and novel electric motor designs are needed to overcome these technological challenges and meet these goals.

Modeling of electric motors has in the past been studied predominantly by the electrical engineering community. The focus has been on the calculation of the magnetic field and resulting torque and iron losses for different motor designs using both analytical, (e.g. see: Boules (1984); Zhu et al. (1993); Lubin et al. (2011); Devillers et al. (2016)) and numerical (e.g. see: Chari and Silvester (1971); Silvester et al. (1973); Abdel-Razek et al. (1982); Arkkio (1987); Huppunen et al. (2004)) methods. By the late 90s, stress calculations in electric motors started appearing as a result of noise and vibrations concerns. The first FEM computations for stresses in electric motors used a stepwise, uncoupled, approach: electric currents and magnetic fields where calculated using a purely electromagnetic model; the electromagnetic body force vector – a source of confusion, due to the many different expressions adopted in the corresponding literature – was then introduced as the external body force in a purely mechanical model to calculate the resulting stress state (e.g. see: Reyne et al. (1988); Javadi et al. (1995); Vandevelde et al. (2004)).

The above-described approximate methods are inadequate to deal with the true multiphysics nature of the electric motor problem. In particular these materials exhibit a strongly coupled magnetic and mechanical behavior, with the material magnetization influencing the stress state via the "*magnetostriction*" phenomenon and the stress state of the material also impacting its magnetization via "*inverse magnetostriction* (Daniel et al., 2020). Recognizing these issues, recent work by Fonteyn et al. (2010a,b) takes into account magnetoelastic coupling effects for the numerical stress calculation in electric motors. However several approximations are used: i.e. a small strain approximation involving non frame-indifferent invariants and the angular momentum balance principle is not imposed.

To overcome the above-mentioned difficulties in the correct modeling of stresses in electrical motors, the authors recently proposed in Hanappier et al. (2021a) a multiphysics setting for the equations governing electric motors. Using the direct approach of continuum mechanics, a general framework that couples the electromagnetic, thermal and mechanical fields is derived using the basic principles of thermodynamics. Particular attention is paid to the derivation of the coupled constitutive equations for isotropic materials under small strain but arbitrary magnetization, which is relevant for typical electric motors. As an application, analytical solutions of idealized rotor and stator problems are presented, respectively in Hanappier et al. (2021a) and Hanappier et al. (2021b).

For more realistic motor problems, numerical solutions of the governing equations are in order to account

for the complex geometry of a typical electric motor and the coupled magneto-mechanical non-linear material behavior. To this end, a Lagrangian[1] (reference configuration) variational approach is proposed for the eddy current approximation that properly retrieves the Maxwell stresses and is consistent with its direct approach counterpart. Based on this variational principle, a numerical (FEM) discretization algorithm is proposed in the present work and subsequently applied to the solution of different stator boundary value problems.

The outline of the presentation is a follows: after the motivation in Section 1, the presentation continues with a brief description of a typical electric motor boundary value problem in Section 2 followed by the general variational theory of the eddy current approximation in Section 3. The numerical implementation is given in Section 4 followed by the applications in Section 5. Specifically, the proposed method is first applied to a cylindrical stator, where an analytical solution can be found for the linear magnetization regime, thus providing firstly an independent code verification and subsequently an assessment of the influence of the stator's nonlinear magnetic response. The approach is subsequently used to tackle a realistic stator geometry with two pole pairs under a three-phase current for two different cases: loosely or tightly packed conducting wires, to calculate the corresponding magnetic and stress fields. Conclusion is presented in Section 6. The analytical solution of the cylindrical stator problem with a linear elastic and magnetic responses is given in Appendix A with the derivation of the force vector and stiffness matrix for the FEM discretization of the variational principle following in Appendix B.

2. Brief description of the electric motor problem

To set the stage we start by showing the cross-section of a typical motor, consisting of a turning part, termed "*rotor*" and a fixed part, termed "*stator*" separated by an "*airgap*", as seen in Figure 1 that shows a typical electric motor's complex geometry.

[1] For a details on the equivalence between the Lagrangian variational approach and the Eulerian direct approach in the most general setting, the reader is directed to Hanappier (2021).

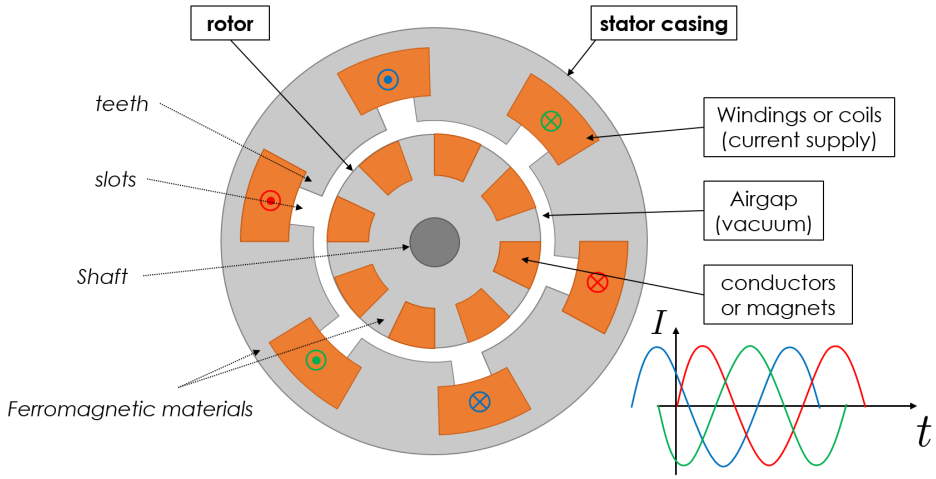

Figure 1: Cross-section of a typical asynchronous motor, showing rotor, airgap and stator, with current supply coil domains.

Stator windings or coils are supplied by phase-shifted, alternating currents to create a rotating magnetic field. The rotor can have permanent magnets or conducting bars (cage rotor). It can also be made of a plain ferromagnetic material in the case of high speed machines. When the rotor has magnets, the motor is called "*synchronous*" since the rotor spins at the same frequency as the stator magnetic field. Motors having rotors with conducting bars or plain ferromagnetic (but without magnets) rely on induction: the rotating stator field induces currents at the rotor, which in turn trigger Lorentz forces creating the rotor motion. An angular velocity differential, called "*slip*", between the rotor and the stator results and the motor is called "*asynchronous*". The dark region at the center of the rotor indicates the motor shaft, which transmits the mechanical load (torque). The bulk of the rotor and stator are usually made of ferromagnetic materials with high magnetic susceptibility to enhance and channel the magnetic flux. The ferromagnetic materials used to strongly enhance the magnetic field, exhibit a non-linear (in particular magnetic) material behavior as well as magneto-mechanical coupling.

3. Theory: variational formulation for the eddy current approximation

We start with the general variational formulation of the coupled electro-magneto-mechanical problem using the eddy current approximation, after Thomas and Triantafyllidis (2009). Following the introduction of the appropriate Lagrangian and Hamilton's functionals in subsection 3.1, we show how the stationarity of the latter imposes the vanishing of its variations with respect to the magnetic potential $\boldsymbol{A}$ and the displacement $\boldsymbol{u}$, in subsections 3.2 and 3.3. We thus obtain respectively the field equations and boundary/interface conditions for the magnetic and mechanical response of the solid as well as the magnetic field in the airgap.

A comment on notation is in order at this point: coordinate-free (dyadic) continuum mechanics notation is used with bold symbols referring to tensors and script ones to scalars. The FEM calculations are performed in a Lagrangian setting using the unloaded configuration as reference. Unless stated otherwise, all field quantities are functions of the reference position $\boldsymbol{X}$ and time t. Lagrangian field quantities are denoted by capital letters, e.g. magnetic potential $\boldsymbol{A}$, magnetic flux $\boldsymbol{B}$, h-field $\boldsymbol{H}$, current density $\boldsymbol{J}$, first Piola-Kirchhoff stress $\boldsymbol{\Pi}$, while their corresponding Eulerian counterparts are denoted by script letters, e.g. $\boldsymbol{a}$, magnetic flux $\boldsymbol{b}$, h-field $\boldsymbol{h}$, current density $\boldsymbol{j}$, Cauchy stress $\boldsymbol{\sigma}$. For the case of small strains, i.e. $\boldsymbol{F} \approx \boldsymbol{I}$[2], these fields tend to coincide allowing for the comparison between the analytical results in Hanappier et al. (2021b) and the numerical ones presented here.

3.1. Lagrangian and Hamilton functionals

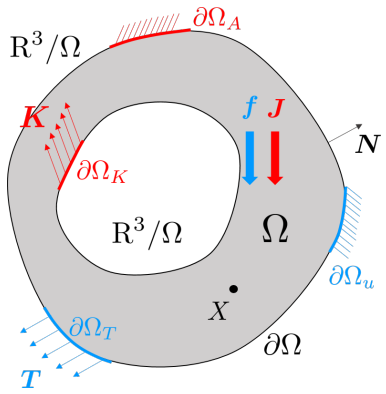

Figure 2: Schematics of the boundary value problem for an electric motor component (reference configuration).

The schematics of the general boundary value problem are given in Figure 2. The solid occupies a volume Ω in the reference configuration with boundary $\partial\Omega$. The solid is subjected to an externally applied reference current density $\boldsymbol{J}$ and an externally applied mechanical body force (per unit mass) $\boldsymbol{f}$. On the boundary we apply a mechanical traction $\boldsymbol{T}$ (per unit reference surface area) and an electric current sheet $\boldsymbol{K}$ (per unit reference surface area). In general surface tractions and current sheet are applied on different parts of the boundary $\partial\Omega_T$ and $\partial\Omega_K$; displacement $\boldsymbol{u}$ and magnetic potential $\boldsymbol{A}$[3] can also be applied on different parts of the boundary $\partial\Omega_u$ and $\partial\Omega_A$ respectively.

Neglecting the electric charge and the electric field energy contributions, the reference configuration "*Lagrangian density*" $\mathscr{\ell}$ (per unit reference volume) for the eddy current approximation (see Thomas and

[2]The capital-script letter rule is not applicable to field quantities relating the two configurations, where no ambiguity is possible and hence the usual standard notation is adopted, i.e. $\boldsymbol{F}$ for the deformation gradient or $\boldsymbol{u}$ for the displacement field.

[3]The Dirichlet condition in magnetics consists of prescribing $\boldsymbol{N} \times \boldsymbol{A}$.

Triantafyllidis (2009)) is given by

$$\ell \equiv -\frac{1}{2\mu_0 J}\boldsymbol{B}\cdot\boldsymbol{C}\cdot\boldsymbol{B} + \boldsymbol{J}\cdot\boldsymbol{A} - \rho_0\psi + \frac{1}{2}\rho_0(\dot{\boldsymbol{u}}\cdot\dot{\boldsymbol{u}}) + \rho_0\boldsymbol{f}\cdot\boldsymbol{u}\ ; \quad \boldsymbol{B} \equiv \boldsymbol{\nabla}\times\boldsymbol{A}\ ,\ \boldsymbol{C} \equiv \boldsymbol{F}^T\cdot\boldsymbol{F}\ , \tag{3.1}$$

where $\boldsymbol{B}$ the reference magnetic field, $\boldsymbol{A}$ the reference magnetic potential[4], $\psi(\boldsymbol{C},\boldsymbol{B})$[5] the specific (per unit mass) Helmholtz free energy and $\boldsymbol{C}$ the right Cauchy-Green tensor, expressed in terms of the deformation gradient $\boldsymbol{F}$. Following standard notation, ρ_0 is the reference mass density of the solid and $\dot{\boldsymbol{u}}$ denotes the time-derivative (velocity) of the displacement $\boldsymbol{u}$. Moreover, μ_0 is the magnetic permeability of vacuum and $J = \det(\boldsymbol{F})$ denotes the deformation-induced volume change.

Based on (3.1), the reference configuration "*total Lagrangian*" $\mathscr{L}$ of the system becomes[6]

$$\mathscr{L} \equiv \int_{\mathbb{R}^3} \ell \ \mathrm{d}V + \int_{\partial\Omega} (\boldsymbol{T}\cdot\boldsymbol{u} + \boldsymbol{K}\cdot\boldsymbol{A})\ \mathrm{d}S\ . \tag{3.2}$$

We also generalize the reference mass density ρ_0 in the definition of the Lagrangian density ℓ in (3.1) over the entire space $\mathbb{R}^3$ as follows: $\rho_0(\boldsymbol{X}) \neq 0$ for $\boldsymbol{X} \in \Omega$ and $\rho_0(\boldsymbol{X}) = 0$ for $\boldsymbol{X} \in \mathbb{R}^3\backslash\Omega$. Integration over $\mathbb{R}^3$ is necessary to account for the electromagnetic field in both the body Ω and its surrounding space $\mathbb{R}^3\backslash\Omega$.

We proceed with the definition of the "*action integral*" $\mathscr{F}(\boldsymbol{A},\boldsymbol{u})$, obtained by integration of the Lagrangian $\mathscr{L}$ in (3.2) between arbitrary times t_1 and t_2. By Hamilton's principle it is stationary

$$\mathscr{F}(\boldsymbol{A},\boldsymbol{u}) \equiv \int_{t_1}^{t_2} \mathscr{L}\ \mathrm{d}t\ , \quad \delta\mathscr{F} = 0\ ; \quad \delta\boldsymbol{A}(t_i) = \delta\boldsymbol{u}(t_i) = \boldsymbol{0}\ ,\ i = 1,2 \implies \mathscr{F}_{,\boldsymbol{A}}[\delta\boldsymbol{A}] = \mathscr{F}_{,\boldsymbol{u}}[\delta\boldsymbol{u}] = 0\ . \tag{3.3}$$

Consequently the corresponding variations with respect to the independent variables $\boldsymbol{A}$ and $\boldsymbol{u}$ yield respectively the magnetic and mechanical governing equations and interface/boundary conditions.

3.2. Magnetics: variations with respect to $\boldsymbol{A}$

Following (3.3), setting to zero the variation of $\mathscr{F}$ with respect to $\boldsymbol{A}$ one obtains

$$\mathscr{F}_{,\boldsymbol{A}}[\delta\boldsymbol{A}] = \int_{t_1}^{t_2} \left\{ \int_{\mathbb{R}^3} \left[\boldsymbol{J}\cdot\delta\boldsymbol{A} - \frac{1}{\mu_0}(\boldsymbol{B}\cdot\boldsymbol{C})\cdot(\boldsymbol{\nabla}\times\delta\boldsymbol{A}) - \rho_0\frac{\partial\psi}{\partial\boldsymbol{B}}\cdot(\boldsymbol{\nabla}\times\delta\boldsymbol{A}) \right] \mathrm{d}V \right\} \mathrm{d}t + \int_{\partial\Omega} (\boldsymbol{K}\cdot\delta\boldsymbol{A})\ \mathrm{d}S = 0\ . \tag{3.4}$$

[4] An additional condition is needed for a unique $\boldsymbol{A}$, termed "*gauge condition*"; Coulomb gauge $\boldsymbol{\nabla}\cdot\boldsymbol{A} = 0$ is a typical choice.

[5] Dissipative phenomena (e.g. magnetic hysteresis or plasticity) are ignored and thus no internal variables are needed in ψ. Temperature dependance is ignored as well. The specific free energy used here depends on $(\boldsymbol{C}, \boldsymbol{B} = J\boldsymbol{F}^{-1}\cdot\boldsymbol{b})$, as opposed to $(\boldsymbol{C}, \boldsymbol{b}\cdot\boldsymbol{F})$ in Kovetz (2000); Hanappier et al. (2021a,b). Our choice, motivated by the fact that $\boldsymbol{B}$ is the Lagrangian counterpart of Eulerian $\boldsymbol{b}$, still complies with the angular momentum balance argument made in Kovetz (2000). For a detailed explanation of this point, see Hanappier (2021).

[6] Without loss of generality, we can define the applied mechanical traction $\boldsymbol{T}$ and current sheet $\boldsymbol{K}$ fields on the entire boundary and impose a zero value when applicable

The domain $\mathbb{R}^3$ is separated into the volume Ω occupied by the body and the surrounding space $\mathbb{R}^3\backslash\Omega$. Taking into account the discontinuity of ρ_0 across $\partial\Omega$, integration by parts of (3.4) yields

$$\mathscr{F}_{,\boldsymbol{A}}[\delta\boldsymbol{A}] = \int_{t_1}^{t_2} \left\{ \int_{\mathbb{R}^3} \left[(\boldsymbol{J} - \boldsymbol{\nabla}\times\boldsymbol{H})\cdot\delta\boldsymbol{A} \right] \mathrm{d}V + \int_{\partial\Omega} \left[(\boldsymbol{K} - \boldsymbol{N}\times[\![\boldsymbol{H}]\!])\cdot\delta\boldsymbol{A} \right] \mathrm{d}S \right\} \mathrm{d}t = 0 \,,$$

$$\boldsymbol{H} \equiv -\frac{\partial\mathscr{\ell}}{\partial\boldsymbol{B}} = \begin{cases} \rho_0 \dfrac{\partial\psi}{\partial\boldsymbol{B}} + \dfrac{1}{\mu_0 J}\boldsymbol{C}\cdot\boldsymbol{B} \,; \quad \forall\, \boldsymbol{X}\in\Omega \,, \\ \\ \dfrac{1}{\mu_0 J}\boldsymbol{C}\cdot\boldsymbol{B} \,; \quad \forall\, \boldsymbol{X}\in\mathbb{R}^3\backslash\Omega \,, \end{cases} \tag{3.5}$$

where $\boldsymbol{H}$ is the reference configuration h-field"[7]. The arbitrariness of $\delta\boldsymbol{A}$, (3.5) implies the following differential equation and boundary/interface condition

$$\boldsymbol{\nabla}\times\boldsymbol{H} = \boldsymbol{J} \,; \quad \forall\boldsymbol{X}\in\mathbb{R}^3 \,, \qquad \boldsymbol{N}\times[\![\boldsymbol{H}]\!] = \boldsymbol{K} \,; \quad \forall\boldsymbol{X}\in\partial\Omega \,, \tag{3.6}$$

where one recognizes the reference configuration Maxwell-Ampère law in the eddy current approximation (see Hanappier (2021)).

3.3. Mechanics: variations with respect to $\boldsymbol{u}$

Once again, from Hamilton's principle (3.3), setting to zero the variation of $\mathscr{F}$ with respect to $\boldsymbol{u}$ gives

$$\begin{aligned} \mathscr{F}_{,\boldsymbol{u}}[\delta\boldsymbol{u}] = \int_{t_1}^{t_2} \Bigg\{ \int_{\mathbb{R}^3} \Bigg[\left(\frac{1}{\mu_0 J} \left(\frac{1}{2}(\boldsymbol{B}\cdot\boldsymbol{C}\cdot\boldsymbol{B})\boldsymbol{I} - \boldsymbol{B}(\boldsymbol{C}\cdot\boldsymbol{B}) \right)\cdot\boldsymbol{F}^{-1} - \rho_0 \left(\frac{\partial\psi}{\partial\boldsymbol{C}} \right)\cdot\boldsymbol{F}^T \right) : (\boldsymbol{\nabla}\delta\boldsymbol{u}) \\ + \rho_0\dot{\boldsymbol{u}}\cdot\frac{\mathrm{d}}{\mathrm{d}t}(\delta\boldsymbol{u}) + \rho_0\boldsymbol{f}\cdot\delta\boldsymbol{u} \Bigg] \mathrm{d}V + \int_{\partial\Omega} (\boldsymbol{T}\cdot\delta\boldsymbol{u}) \,\mathrm{d}S \Bigg\} \mathrm{d}t = 0 \,. \end{aligned} \tag{3.7}$$

As before, the domain $\mathbb{R}^3$ is separated into the volume Ω occupied by the body and the surrounding space $\mathbb{R}^3\backslash\Omega$. Taking into account the discontinuity of ρ_0 across $\partial\Omega$, integration by parts of (3.7) in the space and the time domains (recalling also the end conditions at t_1, t_2 in (3.3)) yields

$$\mathscr{F}_{,\boldsymbol{u}}[\delta\boldsymbol{u}] = \int_{t_1}^{t_2} \left\{ \int_{\mathbb{R}^3} \left[(\boldsymbol{\nabla}\cdot\boldsymbol{\Pi} - \rho_0\ddot{\boldsymbol{u}} + \rho_0\boldsymbol{f})\cdot\delta\boldsymbol{u} \right] \mathrm{d}V + \int_{\partial\Omega} \left[(\boldsymbol{T} - \boldsymbol{N}\cdot[\![\boldsymbol{\Pi}]\!])\cdot\delta\boldsymbol{u} \right] \mathrm{d}S \right\} \mathrm{d}t = 0 \,,$$

$$\boldsymbol{\Pi} \equiv -\left(\frac{\partial\mathscr{\ell}}{\partial\boldsymbol{F}} \right)^T = \begin{cases} \rho_0 \left(\dfrac{\partial\psi}{\partial\boldsymbol{C}} \right)\cdot\boldsymbol{F}^T + \dfrac{1}{\mu_0 J}\boldsymbol{B}(\boldsymbol{F}\cdot\boldsymbol{B}) - \dfrac{1}{2\mu_0 J}(\boldsymbol{B}\cdot\boldsymbol{C}\cdot\boldsymbol{B})\boldsymbol{F}^{-1} \,; \quad \forall\, \boldsymbol{X}\in\Omega \,, \\ \\ \dfrac{1}{\mu_0 J}\boldsymbol{B}(\boldsymbol{F}\cdot\boldsymbol{B}) - \dfrac{1}{2\mu_0 J}(\boldsymbol{B}\cdot\boldsymbol{C}\cdot\boldsymbol{B})\boldsymbol{F}^{-1} \,; \quad \forall\, \boldsymbol{X}\in\mathbb{R}^3\backslash\Omega \,, \end{cases} \tag{3.8}$$

[7] The reference and current configuration h-fields are related by $\boldsymbol{H} = \boldsymbol{h}\cdot\boldsymbol{F}$ (see Hanappier (2021)).

where $\boldsymbol{\Pi}$ is the "*total first Piola-Kirchhoff*" stress tensor[8]. The arbitrariness of $\delta\boldsymbol{u}$, (3.8) yields the following differential equation and boundary/interface condition

$$\boldsymbol{\nabla}\cdot\boldsymbol{\Pi} + \rho_0\boldsymbol{f} = \rho_0\ddot{\boldsymbol{u}}\ ; \quad \forall\boldsymbol{X}\in\mathbb{R}^3\ , \qquad \boldsymbol{N}\times[\![\boldsymbol{\Pi}]\!] = \boldsymbol{T}\ ; \quad \forall\boldsymbol{X}\in\partial\Omega\ , \tag{3.9}$$

where one recognizes the reference configuration linear momentum balance of continuum mechanics.

It should be noted here that the present Lagrangian approach enables one to automatically calculate the Maxwell stress in the airgap regions[9] $\mathbb{R}^3\backslash\Omega$, as seen from $(3.8)_3$.

4. Numerical (FEM) implementation

We apply here the general theory developed in Section 3 to the boundary value problem of a stator. The numerical solution is based on an FEM discretization of a 2D, quasistatic problem and solved by extremization of a simplified version of the Lagrangian (3.2). In subsection 4.1 we present the potential energy of the problem and the corresponding field variables. In subsection 4.2 we give the specific free energies used in the calculations and in subsection 4.3 we present some important implementation details.

4.1. Potential energy and field variables

This stator analysis is based on a 2D model (plane strain assumed, see cross-section in Figure 1), where all field quantities are assumed independent of X_3. It involves no external body forces and mechanical tractions and has negligible induced currents and acceleration terms, thus requiring only a spatial discretization of the corresponding quasistatic problem. The Lagrangian of the system (kinetic minus potential energy: $\mathscr{L} = \mathscr{K} - \mathscr{P}$), in the absence of the kinetic energy ($\mathscr{K} = 0$) equals minus the potential energy ($\mathscr{L} = -\mathscr{P}$), which for the case of no external body forces and mechanical surface tractions becomes

$$\mathscr{P} = \int_{\mathbb{R}^2} (\mathscr{p})\ \mathrm{d}S - \int_{\Omega} (\boldsymbol{J}\cdot\boldsymbol{A})\ \mathrm{d}S - \int_{\partial\Omega} (\boldsymbol{K}\cdot\boldsymbol{A})\ \mathrm{d}l\ ; \quad \mathscr{p} \equiv \rho_0\psi + \frac{1}{2\mu_0 J}\boldsymbol{B}\cdot\boldsymbol{C}\cdot\boldsymbol{B}\ , \tag{4.1}$$

where $\mathscr{p}$ is the system's energy density.

Since a plane strain boundary value problem is considered, integration over the entire domain involves $\mathbb{R}^2$ and the cross-section of the stator domain has boundary $\partial\Omega$. Moreover, the in-plane magnetic field ($\boldsymbol{B} = \boldsymbol{\nabla}\times\boldsymbol{A}$, see (3.1)) is derived from the magnetic vector potential $\boldsymbol{A} = A(X_1, X_2)\boldsymbol{e}_3$, requiring only one scalar field variable for its determination i.e. $\boldsymbol{B} = A_{,2}\boldsymbol{e}_1 - A_{,1}\boldsymbol{e}_2$[10]. Consequently the Coulomb gauge condition $\boldsymbol{\nabla}\cdot\boldsymbol{A}$ (see footnote 4) is automatically satisfied. As a result of Ampère's law (3.6) and the in-plane h-field, the externally applied currents can only be of the form $\boldsymbol{J} = J_3(X_1, X_2)\boldsymbol{e}_3$, thus automatically satisfying the charge conservation principle $\boldsymbol{\nabla}\cdot\boldsymbol{J} = 0$.

[8] The total first Piola-Kirchhoff and Cauchy stress tensors are related by $\boldsymbol{\Pi} = J\boldsymbol{F}^{-1}\cdot\boldsymbol{\sigma}$ (see Hanappier (2021)).

[9] This is a more straightforward approach, compared to other methodologies that require adding the Maxwell stress contribution at the interfaces with airgap regions; e.g. Fonteyn et al. (2010b).

[10] The standard partial derivative notation is used $A_{,i} \equiv \partial A/\partial X_i\ ;\ i = 1, 2$

Thus the solution of the stator boundary value problem requires the following three field variables $u_1(X_1, X_2),\ u_2(X_1, X_2),\ A(X_1, X_2)$

$$\boldsymbol{u} = u_1(X_1, X_2)\, \boldsymbol{e}_1 + u_2(X_1, X_2)\, \boldsymbol{e}_2 \ , \quad \boldsymbol{A} = A(X_1, X_2)\, \boldsymbol{e}_3 \ . \tag{4.2}$$

The numerical solution of the problem is based on the FEM spatial discretization of the above three scalar fields, and the derivation of the element force vector and stiffness matrix are presented in Appendix B.

4.2. Constitutive choices

For isotropic materials in 2D, the most general form of their specific free energy[11] can be expressed as a function of only 4 invariants I_1, I_2, J_1 and J_2 (out of the 6 invariants for a 3D isotropic case),

$$\psi(\boldsymbol{C}, \boldsymbol{B}) = \psi(I_1, I_2, J_1, J_2) \ ; \quad I_1 \equiv \mathrm{tr}(\boldsymbol{C}) \ , \ I_2 \equiv \det(\boldsymbol{C}) = J^2 \ , \ J_1 \equiv \boldsymbol{B}\cdot\boldsymbol{B} \ , \ J_2 \equiv \boldsymbol{B}\cdot\boldsymbol{C}\cdot\boldsymbol{B} \ . \tag{4.3}$$

For the e-motor applications of interest here, the specific free energy is decomposed into a purely mechanical part and a magneto-mechanical part (see Hanappier et al. (2021a)),

$$\psi(\boldsymbol{C}, \boldsymbol{B}) = \psi_{mech}(\boldsymbol{C}) + \psi_{mag}(\boldsymbol{C}, \boldsymbol{B}) \ . \tag{4.4}$$

4.2.1. For ferromagnetic materials

Mechanical energy density For the mechanical specific free energy $\psi_{mech}(\boldsymbol{C})$, or equivalently its reference energy density counterpart $W_{mech}(\boldsymbol{C})$, a neo-Hookean behavior is chosen,

$$W_{mech}(I_1, I_2) \equiv \rho_0 \psi_{mech}(I_1, I_2) = G\left[\frac{1}{2}(I_1 - 2 - \ln I_2) + \frac{\nu}{1-2\nu}(\sqrt{I_2} - 1)^2\right] \ , \tag{4.5}$$

where ν denotes the Poisson ratio ($-1 < \nu < 0.5$) and G the shear modulus. More appropriate and refined choices may be relevant for modeling metals (e.g. see Thomas and Triantafyllidis (2009)) but the neo-Hookean model is perfectly adequate here, given the small strains expected Hanappier et al. (2021a).

Magnetic energy density The magnetic specific free energy ψ_{mag}, or equivalently its reference energy density counterpart $W_{mag}(\boldsymbol{C}, \boldsymbol{B})$, pertains to the magnetic response of the steel stator, assuming an anhysteretic magnetic behavior (no dissipative phenomena considered here). For small magnetic fields (and small strains), the model must capture the linear magnetization behavior of the material, i.e. predict its magnetic susceptibility χ[12]. The model should also account for saturation, i.e. asymptotically approach a magnetization m_s at large magnetic fields. To this effect, a model that combines a quadratic energy – linear

[11] A user element is defined for the FEM modeling of the various motor domains, i.e. air, copper conductors and ferromagnetic electrical steel. The specific free energy for each material is assumed isotropic.

[12] It has been shown in Hanappier et al. (2021a) that for small strains and magnetic fields the magnetic response is consistently characterized by two constants: magnetic susceptibility χ - considered here - and magnetostriction Λ - set to zero by selection of the energy density in (4.6).

magnetization – at small $\|\boldsymbol{b}\|$ with a Langevin-type one (e.g. see Danas (2017)) to account for magnetization saturation at high $\|\boldsymbol{b}\|$ is used,

$$\|\boldsymbol{b}\| \leq b_{lim}: \quad W_{mag}(I_2,J_2) = \rho_0\psi_{mag}(I_2,J_2) = -\frac{\chi}{2\mu}\frac{J_2}{I_2}\,; \qquad \mu = \mu_0(1+\chi)\,,$$

$$\|\boldsymbol{b}\| > b_{lim}: \quad W_{mag}(I_2,J_2) = -\frac{\chi}{2\mu}b_{lim}^2 - \frac{\chi}{\mu}\left(\frac{J_2}{I_2} - b_{lim}\right) \tag{4.6}$$

$$+\frac{\alpha_s m_s}{\beta}\left[\ln\left(\beta\left(\sqrt{\frac{J_2}{I_2}} - b_{lim}\right)\right) - \ln\left(\sinh\left(\beta\left(\sqrt{\frac{J_2}{I_2}} - b_{lim}\right)\right)\right)\right]\,; \quad \beta \equiv \frac{3}{\alpha_s m_s}\frac{\chi}{\mu}\,,$$

where m_s is the magnetization at saturation, and α_s is a correction coefficient introduced to obtain a better fit to experimental data (see Section 5). It should be noted here that the isotropic magnetic energy density in (4.6) depends solely on the magnitude of the current magnetic field, i.e. $W_{mag}(I_2,J_2) = W_{mag}(\|\boldsymbol{b}\|)$, since $\boldsymbol{B} = J\boldsymbol{F}^{-1}\cdot\boldsymbol{b} \implies \boldsymbol{b}\cdot\boldsymbol{b} = J_2/I_2$.

For small strains – typical in electric motors – i.e. when $\|\boldsymbol{\epsilon}\| \ll 1$, where $\boldsymbol{\epsilon} \equiv (1/2)(\boldsymbol{\nabla u} + \boldsymbol{u\nabla})$, but arbitrary magnetic field amplitudes $\|\boldsymbol{b}\|$, the present choice of specific free energy matches the small strain magnetization and stress expressions presented in Hanappier et al. (2021a). In particular, the total stress $\boldsymbol{\sigma}$ ($\approx \boldsymbol{\Pi}$) is the sum of a purely elastic part $\overset{e}{\boldsymbol{\sigma}}(\boldsymbol{\epsilon})$ and a purely magnetic part $\overset{m}{\boldsymbol{\sigma}}(\boldsymbol{b})$

$$\boldsymbol{\sigma} = \overset{e}{\boldsymbol{\sigma}} + \overset{m}{\boldsymbol{\sigma}}\,;\ \overset{e}{\boldsymbol{\sigma}} \equiv \lambda\mathrm{tr}(\boldsymbol{\epsilon})\boldsymbol{I} + 2G\boldsymbol{\epsilon}\,,\ \overset{m}{\boldsymbol{\sigma}} \equiv \frac{1}{\mu_0}\left[\boldsymbol{bb} - \frac{1}{2}(\boldsymbol{b}\cdot\boldsymbol{b})\boldsymbol{I}\right] - \frac{\chi(\|\boldsymbol{b}\|)}{\mu(\|\boldsymbol{b}\|)}\left[\boldsymbol{bb} - (\boldsymbol{b}\cdot\boldsymbol{b})\boldsymbol{I}\right] + \frac{\Lambda(\|\boldsymbol{b}\|)}{\mu(\|\boldsymbol{b}\|)}\boldsymbol{bb}\,, \tag{4.7}$$

$$\boldsymbol{m} = [\chi(\|\boldsymbol{b}\|)/\mu(\|\boldsymbol{b}\|)]\,\boldsymbol{b}\,, \quad \mu(\|\boldsymbol{b}\|) = \mu_0[1+\chi(\|\boldsymbol{b}\|)]\,,$$

where $\chi(\|\boldsymbol{b}\|)$ is the material's *magnetic susceptibility*, $\mu(\|\boldsymbol{b}\|)$ its *magnetic permeability* and $\Lambda(\|\boldsymbol{b}\|)$ a *magneto mechanical coupling* coefficient which gives the curvature of the strain vs magnetic field in a stress-free uniaxial magnetostriction experiment. For the magnetic energy adopted in (4.6), $\Lambda(\|\boldsymbol{b}\|) = 0$.

4.2.2. For airgap and conductor domains

For airgap domain, $W_{mag} = 0$ but a penalty-type method, with a mechanical energy density $W_{mech} \neq 0$ is adopted (see Thomas and Triantafyllidis (2009)) to obtain continuous displacement fields. We assume $G_{air} = 10^{-5}G_{steel}$ while keeping the Poisson ratio ν the same as in the steel stator.

For the coil conductor's domain (typically made of copper, a non-magnetic material), we also take $W_{mag} = 0$. The selection of its mechanical energy density is more complicated, as this domain is not monolithic but consists of wires in contact with each other and the stator. Two limiting cases are thus considered for this domain's W_{mech}: i) for the case of "*loosely packed conductors*" and not in contact with the stator, we neglect the stiffness of the copper wire domain by taking $G_{copper} = G_{air} = 10^{-5}G_{steel}$ and ii)

for the case of "*tightly packed conductors*" in contact with the stator, we assume a monolithic copper domain bonded to the stator, in which case we use the corresponding values of the shear modulus and Poisson ratio.

4.3. FEM discretization

For the sake of simplicity and meshing flexibility, the elements chosen for the FEM spatial discretization are constant strain triangular 2D elements; the sole numerical integration point being at the element centroid. The three degrees of freedom of node i are $\boldsymbol{q}^{(i)} = (u_1^{(i)}, u_2^{(i)}, A^{(i)})$ and the corresponding element force vector $\boldsymbol{f}_e$ and element stiffness matrix $\boldsymbol{k}_e$ are derived in Appendix B. The corresponding UEL (user element) is provided to "*Abaqus*" in the final assembly of the global force vector and stiffness matrix of the problem.

5. Simulation of electric stators

Results obtained for the multiphysics modeling of stators, using the numerical implementation described in Section 4, are presented here in two parts. In subsection 5.1 an idealized (cylindrical) rotor is solved using the FEM code[13]. We present the results for the nonlinear magnetic response in (4.6) and we assess its influence by comparing the FEM results to the corresponding analytical solution of Hanappier et al. (2021b). In subsection 5.2, numerical results are presented using the same constitutive laws but a more realistic stator geometry inspired from Devillers et al. (2018b) that includes teeth and slots.

An important point needs to be made here: although the numerical calculations are done in a full Lagrangian setting, due to the small strains, results are expressed in the current configuration, i.e. $\boldsymbol{A} \approx \boldsymbol{a}$, $\boldsymbol{B} \approx \boldsymbol{b}$, $\boldsymbol{H} \approx \boldsymbol{h}$, $\boldsymbol{\Pi} \approx \boldsymbol{\sigma}$.

[13]For code validation and accuracy checking, the FEM results are compared to the analytical results in Hanappier et al. (2021b) obtained for small values of the magnetic field (linear range of magnetic behavior).

5.1. Results for an idealized (cylindrical) stator problem

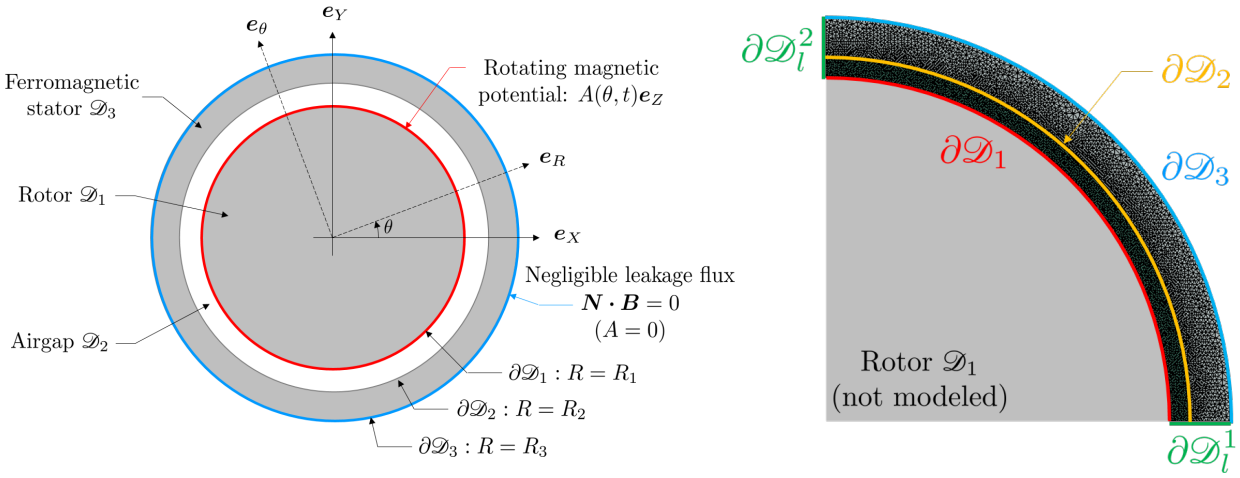

(a) schematics of the idealized (cylindrical stator) motor

(b) FEM mesh of quarter idealized stator

Figure 3: In (a) cross-section of the idealized (cylindrical stator) electric motor, indicating rotor, airgap and stator domains and associated boundaries and in (b) FEM mesh used for modeling the quarter domain of the idealized stator.

Geometry The idealized motor geometry is shown in Figure 3a and its dimensions are given in Table 4a. Because of the symmetries in the geometry – and in the subsequently defined loading – only a quarter domain is discretized, as shown in Figure 3b which also introduces the labelling of the different domains and their boundaries. The unstructured mesh consists of 27,783 elements with 14,794 nodes and 44,382 d.o.f.; the mesh is optimized for accuracy using the analytical solution for the linear magnetic response.

Geometry		
Rotor bore radius	R_1	42.5 mm
Stator yoke bore radius	R_2	45 mm
Stator outer radius	R_3	50 mm
Number of pole pairs	p	2
Loading		
Magnetic field amplitude	B_0	0.23 $\mu_0 m_s$
Material		
Initial magnetic susceptibility	χ	$2,500$
Magnetization at saturation	m_s	1.30×10^6 A/m
Transition from linear regime	b_{lim}	$55\%\mu_0 m_s \approx 0.9$T
Correction coefficient	α_s	3.8
Mass density	ρ_0	$7,650$ kg/m^3
Young's modulus	E	215×10^9 Pa
Poisson ratio	ν	0.3

(a) Geometry, loading and material table.

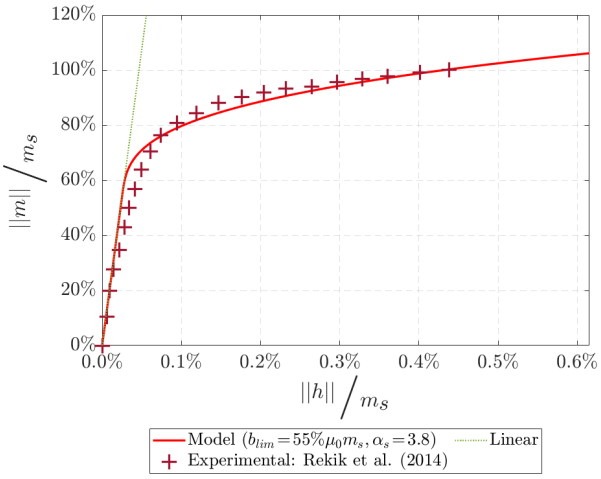

(b) Fitting (4.6) to the experimental $m-h$ curve.

Figure 4: Table of geometry, loading parameter and material properties for the cylindrical rotor in (a) and fitting of the magnetic constitutive law in (4.6) to the experimental $m-h$ results of Rekik et al. (2014) in (b).

Materials Table 4a records the material parameters of the cylindrical stator. The nonlinear description of the magnetic response in (4.6) requires, in addition to the magnetic susceptibility χ, two more parameters: the magnetization at saturation m_s and the correction coefficient α_s. The saturation value $m_s = 1.3\times10^6$ is taken as the maximum magnetization reported in the experimental data of Rekik et al. (2014)[14]. The best fit to the experimental data reported there correspond to a correction factor $\alpha_s = 3.8$ and a transition magnetic field $b_{lim} = 55\%\mu_0 m_s$, as seen in Figure 4b.

Loading The rotor comprises p-pairs ($p = 2$ here) of permanent magnets that produce a rotating radial magnetic field $B_r = -B_0 \sin(p\theta - p\Omega t)$ at the rotor boundary $\mathscr{D}_1$, with B_0 the amplitude of the field and Ω the angular velocity of the rotor. The FEM results obtained here correspond to a snapshot at time $t = 0$; the solution at any time t is obtained by a rotation by an angle Ωt.

We proceed next by recording the essential (Dirichlet) magnetic and mechanical boundary conditions imposed. The maximum amplitude B_0 is chosen so that the numerically calculated magnetization nowhere exceeds its saturation value, thus operating within the range of the fitted magnetic response, as shown in

[14]We use the data for the unstressed configuration (Figure 11(a) of Rekik et al. (2014) with – following their notations – $\sigma_1 = \sigma_2 = 0$).

Figure 4b and hence justifying the adopted value $B_0 = 0.23\mu_0 m_s$ in Table 4a.

Magnetic boundary conditions Magnetic loading is imposed by prescribing the magnetic potential A at the outer boundary of the rotor

$$\partial\mathscr{D}_1 : \qquad A = \frac{R_1 B_0}{p}\cos(p\theta) \; . \tag{5.1}$$

On the outer boundary of the stator the magnetic potential A is prescribed

$$\partial\mathscr{D}_3 : \qquad A = 0 \; . \tag{5.2}$$

From the above condition we conclude that the radial component of the magnetic field vanishes ($(\partial A/\partial\theta)/R = B_r = \boldsymbol{N}\cdot\boldsymbol{B} = 0$), thus explaining the term "*negligible magnetic leakage flux condition*" recorded in Figure 3a. No essential boundary conditions are imposed on the lateral boundaries $\partial\mathscr{D}_l^1, \partial\mathscr{D}_l^2$ due to the symmetry of the geometry and loading. The corresponding natural (Neumann) boundary condition is $\boldsymbol{N}\times\boldsymbol{H} = -H_r\boldsymbol{e}_z = 0$.

Mechanical boundary conditions Displacements are set to zero on the inner boundary of the airgap $\partial\mathscr{D}_1$.

$$\partial\mathscr{D}_1 : \qquad u_r = u_\theta = 0 \; . \tag{5.3}$$

Moreover, given the symmetries of the geometry and loading, we need only prescribe the tangent displacements on the lateral surfaces $\partial\mathscr{D}_l^1, \partial\mathscr{D}_l^2$, and hence

$$\partial\mathscr{D}_l^1, \; \partial\mathscr{D}_l^2 : \qquad u_\theta = 0 \; . \tag{5.4}$$

The corresponding natural Neumann boundary conditions provide on $\partial\mathscr{D}_l^1$ and $\partial\mathscr{D}_l^2$: $\Pi_{r\theta} = 0$. Since no displacement constraints are imposed on the outer stator boundary, the corresponding natural (Neumann) boundary conditions are on $\partial\mathscr{D}_3 : \sigma_{rr} \approx \Pi_{rr} = 0 \; , \sigma_{r\theta} \approx \Pi_{r\theta} = 0$.

Normalization In order to present results in dimensionless form, the following normalization is adopted using magnetic saturation,

$$a_{ref} = R_2\mu_0 m_s \; , \quad b_{ref} = \mu_0 m_s \; , \quad h_{ref} = m_{ref} = m_s \; , \quad u_{ref} = R_{ref} = R_2 \; , \quad \sigma_{ref} = \mu_0 m_s^2 \; . \tag{5.5}$$

The results of the FEM calculations for the magnetic constitutive law of (4.6) and their comparison to the predictions of the analytic model (magnetic susceptibility $\chi = 2,500$ and magneto-mechanical coupling coefficient $\Lambda = 0$ – see Appendix A), are presented at three different radial directions: $\theta = 0, \; \pi/8, \; \pi/4$, in Figures 5 to 8.

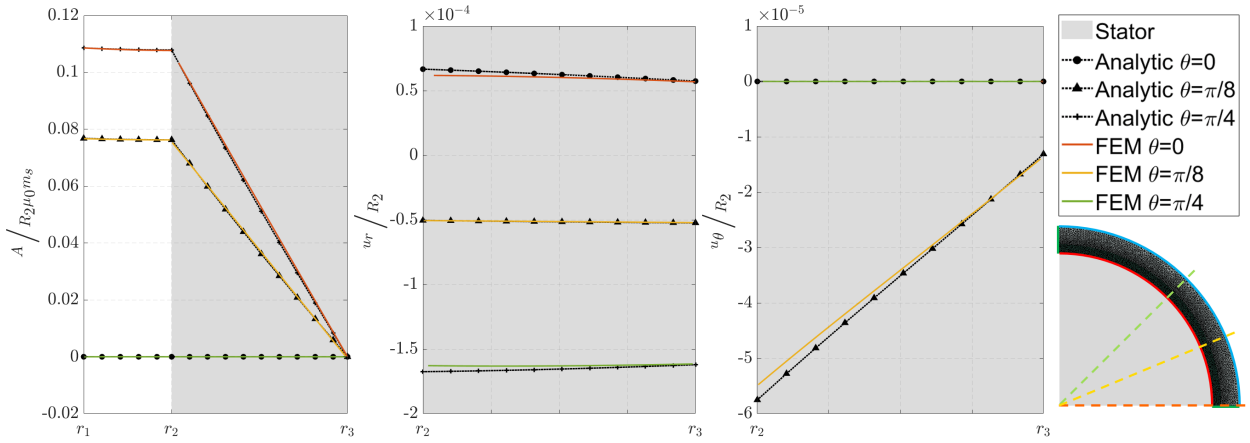

(a) $A/R_2\mu_0 m_s$ vs R/R_2 (b) u_r/R_2 vs R/R_2 (c) u_θ/R_2 vs R/R_2 (d) Labeling

Figure 5: Difference between FEM (nonlinear magnetization response) and analytical predictions (linear magnetization response) for the cylindrical stator at large values magnetic field $\|\boldsymbol{b}\|$ at three different angles. In (a) dimensionless magnetic potential $A/R_2\mu_0 m_s$ vs r, in (b) dimensionless radial displacement u_r/R_2 vs r and in (c) dimensionless tangential displacement u_θ/R_2 vs r (dimensionless radius $r = R/R_2$).

More specifically Figure 5a shows the influence of the nonlinear magnetic response on the dimensionless magnetic potential $A/R_2\mu_0 m_s$ and Figures 5b and 5c show the corresponding effect on the dimensionless radial and tangent displacement components, respectively u_r/R_2 and u_θ/R_2, as functions of the radial coordinate r. According to Figure 5a, there is no (discernible) influence of the nonlinear magnetic response on the potential A. The maximum difference for the radial displacement u_r occurs, according to Figure 5b along the radial directions $\theta = 0,\ \pi/4$ at the inner boundary of the stator ($r_2 = 1$), but the change from the linear model predictions is negligible. Similar results are found for the hoop displacement u_θ in Figure 5c where a (negligible) maximum difference occurs again at the inner boundary of the stator but along the direction $\theta = \pi/8$ (from symmetry $u_\theta = 0$ along $\theta = 0,\ \pi/4$). It should be noted here that for the values selected in Table 4a, the displacements are at most of order 10^{-5}m. One can thus conclude from Figures 5b and 5c that the influence of nonlinear magnetic effects on the mechanical response of the stator is negligible, even for magnetic fields up to saturation level.

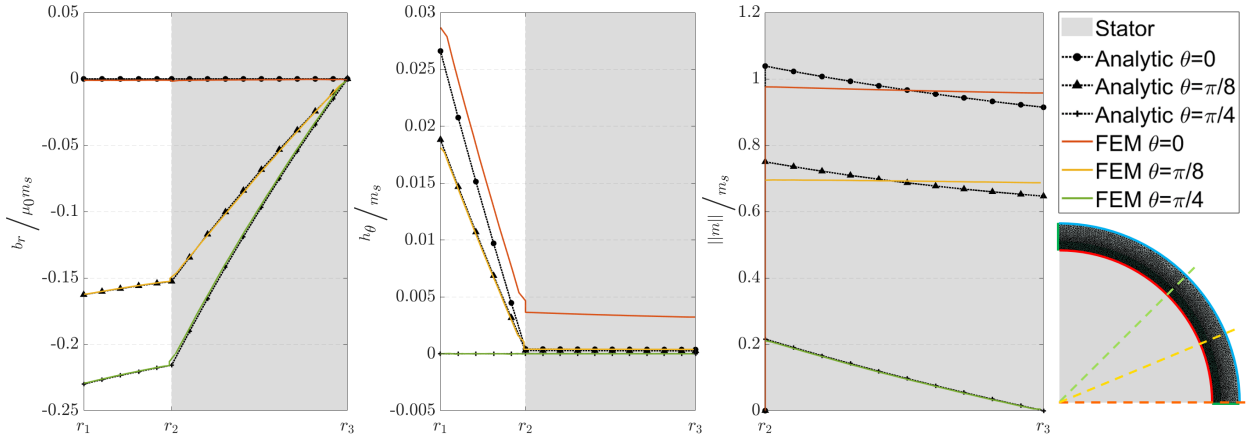

(a) $b_r/\mu_0 m_s$ vs R/R_2 (b) h_θ/m_s vs R/R_2 (c) $\|\boldsymbol{m}\|/m_s$ vs R/R_2 (d) Labeling

Figure 6: Difference between FEM (nonlinear magnetization response) and analytical predictions (linear magnetization response) for the cylindrical stator at large values magnetic field $\|\boldsymbol{b}\|$ at three different angles. In (a) dimensionless radial component of the magnetic field $b_r/\mu_0 m_s$ vs r, in (b) dimensionless tangential component of the h-field h_θ/m_s vs r and in (c) dimensionless norm of the magnetic field $\|\boldsymbol{m}\|/m_s$ vs r (dimensionless radius $r = R/R_2$).

The above assertion – of a negligible influence of the nonlinear magnetic behavior on the stator's mechanical response – is no longer valid for its magnetic counterpart, as seen from Figure 6. The influence of nonlinear magnetic response on the dimensionless magnetic field $b_r/\mu_0 m_s$ is presented in Figure 6a, on the tangential component of the h-field h_θ/m_s in Figure 6b[15] and on the norm of magnetization vector $\|\boldsymbol{m}\|/m_s$ in Figure 6c, as functions of the radial coordinate r. The maximum deviations from the linear response occur, as expected, at the inner boundary of the stator ($r_2 = 1$) where the magnetic field is the highest. Unlike the radial component of the magnetic field b_r that is unaffected by the nonlinear magnetic behavior – as evidenced by Figure 6a – the tangential component h_θ and the magnetization norm $\|\boldsymbol{m}\|$ are influenced by it as seen from Figures 6b and 6c. In particular notice from Figure 6c that the linear magnetic model (constant magnetic susceptibility χ) consistently overestimates/underestimates the magnetization at the inner/outer boundary of the stator, with the nonlinear magnetic model resulting in a more uniform distribution due to saturation.

[15]The reason for plotting the components b_r and h_θ of the magnetic field is to highlight their continuity at the r_2 interface, as expected from the (current configuration) interface conditions $\boldsymbol{n}\cdot[\![\boldsymbol{b}]\!] = 0$ and $\boldsymbol{n}\times[\![\boldsymbol{h}]\!] = \boldsymbol{0}$ respectively.

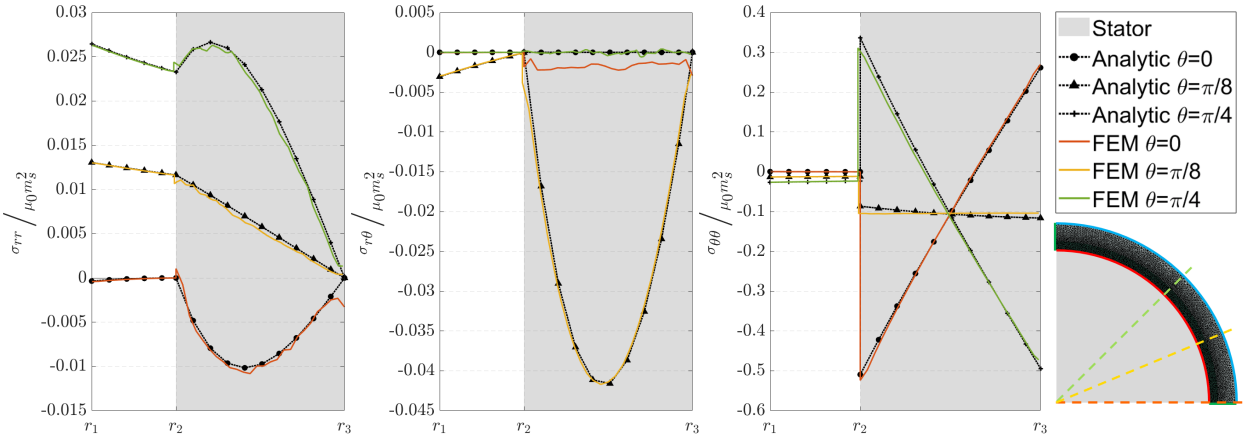

(a) $\sigma_{rr}/\mu_0 m_s^2$ vs R/R_2 (b) $\sigma_{r\theta}/\mu_0 m_s^2$ vs R/R_2 (c) $\sigma_{\theta\theta}/\mu_0 m_s^2$ vs R/R_2 (d) Labeling

Figure 7: Difference between FEM (nonlinear magnetization response) and analytical predictions (linear magnetization response) for the cylindrical stator at large values magnetic field $\|\boldsymbol{b}\|$ at three different angles. In (a) dimensionless radial stress $\sigma_{rr}/\mu_0 m_s^2$ vs r, in (b) dimensionless shear stress $\sigma_{r\theta}/\mu_0 m_s^2$ vs r and in (c) dimensionless hoop stress $\sigma_{\theta\theta}/\mu_0 m_s^2$ vs r (dimensionless radius $r = R/R_2$).

The influence of nonlinear magnetic response on the dimensionless total stress field components is presented in Figure 7. More specifically, Figure 7a shows the magnetically nonlinear (FEM) and linear (analytical) results for the dimensionless normal stress $\sigma_{rr}/\mu_0 m_s^2$, Figure 7b shows the results for the dimensionless shear stress $\sigma_{r\theta}/\mu_0 m_s^2$ and Figure 7c shows the results for the dimensionless hoop stress $\sigma_{\theta\theta}/\mu_0 m_s^2$, as functions of the radial coordinate r. If one disregards the numerical noise of the shear stress $\sigma_{r\theta}$ in the boundary $\theta = 0$[16], the nonlinearity of the magnetic response has negligible influence on the total stress field.

The non-zero total stress (Maxwell stress) in the airgap regions is properly accounted for. Notice in Figures 7a and 7b the continuity of normal σ_{rr} and hoop $\sigma_{r\theta}$ total stress components at the airgap-stator interface, as expected from the current configuration version of the boundary condition $(3.9)_2$ and the absence of an externally applied mechanical surface traction there ($\boldsymbol{T} = \boldsymbol{0}$).

[16]From symmetry $\sigma_{r\theta} = 0$ at $\theta = 0$ but the shear stress is calculated at the midpoint of the boundary elements.

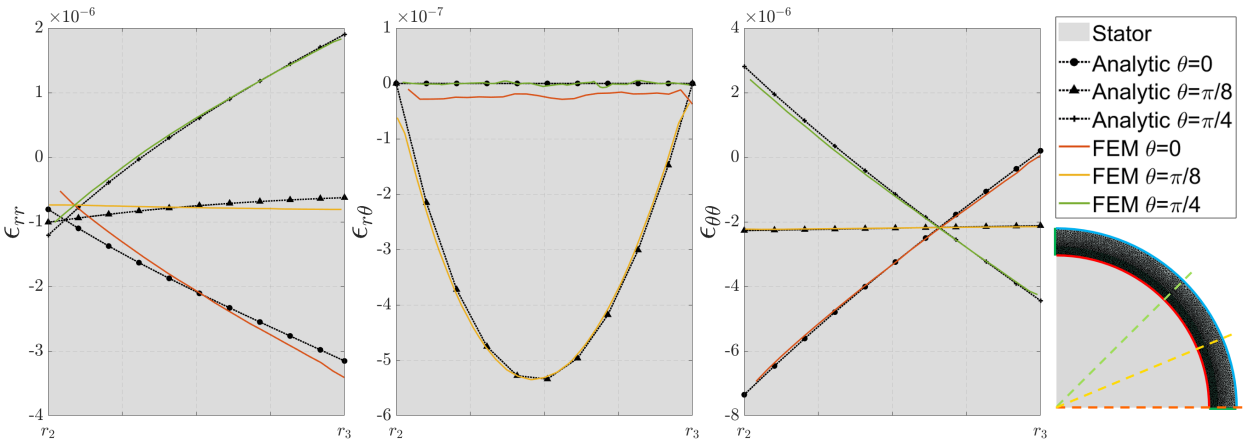

(a) ϵ_{rr} vs R/R_2 (b) $\epsilon_{r\theta}$ vs R/R_2 (c) $\epsilon_{\theta\theta}$ vs R/R_2 (d) Labeling

Figure 8: Difference between FEM (nonlinear magnetization response) and analytical predictions (linear magnetization response) for the cylindrical stator at large values magnetic field $\|\boldsymbol{b}\|$ at three different angles. In (a) radial strain ϵ_{rr} vs r, in (b) shear strain $\epsilon_{r\theta}$ vs r and in (c) hoop strain $\epsilon_{\theta\theta}$ vs r (dimensionless radius $r = R/R_2$).

Finally of interest is the influence of nonlinear magnetic response on the strain field, which is presented in Figure 8. More specifically, Figure 8a shows the magnetically nonlinear (FEM) and linear (analytical) results for the normal strain ϵ_{rr}, Figure 8b shows the results for the shear strain $\epsilon_{r\theta}$ and Figure 8c shows the results for the hoop strain $\epsilon_{\theta\theta}$, as functions of the radial coordinate r. Interest in the strain field stems from its direct relation to the mechanical (elastic) stress field $\overset{e}{\boldsymbol{\sigma}}$ according to (4.7). Notice that although the shear $\epsilon_{r\theta}$ and hoop $\epsilon_{\theta\theta}$ strain fields are not influenced by the nonlinear magnetic response, this is not the case for the radial strain field ϵ_{rr}, as seen in Figure 8a, where the maximum diffence occurs near the stator's inner boundary where the magnetic field is the strongest. Moreover, strains of the order of 10^{-6} correspond to maximum elastic stresses of the order of a few MPa, well within the linear elastic range of the steel's response.

We can conclude that the nonlinear magnetic response of the stator has a rather small influence in the magnetic fields but practically none to the displacement, total stress and strain fields; the (analytically available) linear magnetization model is adequate for the calculation of the kinematic and mechanical fields.

5.2. Results for a realistic geometry stator

Attention is turned next to the FEM simulations for a realistic (slotted) stator geometry. A four-pole (two pairs) induction machine with plain ferromagnetic rotor (as in Hanappier et al. (2021a)) is considered. The stator geometry is inspired by the benchmark machine of Devillers et al. (2018a).

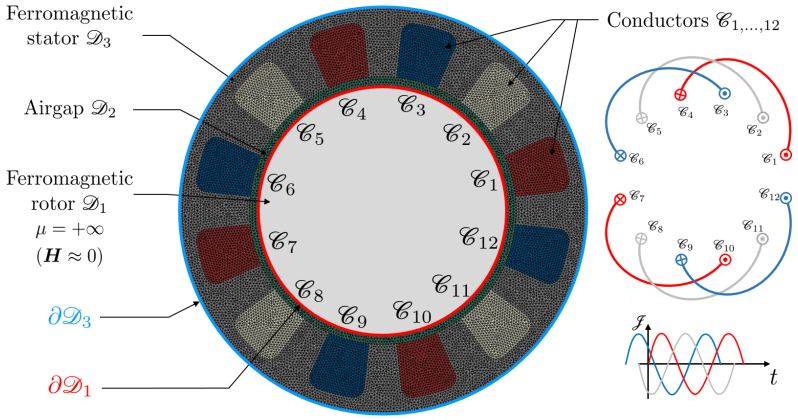

(a) Realistic geometry stator.

Rotor bore radius	R_1	45 mm
Stator bore radius	R_2	48 mm
Stator tooth height	H_{tooth}	20 mm
Stator outer radius	R_3	73 mm
Stator slot width	W_s	18°
Radius at teeth's base	R_b	4mm
Number of stator teeth	Z_s	12
Number of pole pairs	p	2

(b) Stator geometry table.

Figure 9: Realistic geometry stator, mesh and wiring plan; $\otimes$ denotes currents flowing in, and $\odot$ currents flowing out of the plane at a given time (these currents alternate) in (a) and Table of geometric parameters for the realistic stator boundary value problem.

Geometry Figure 9a shows the stator geometry, with the stator domain $\mathscr{D}_3$ in dark grey and the airgap domain $\mathscr{D}_2$ in green[17]. The stator slots hold the conductor coil windings – blue, light gray and red domains in Figure 9a – supplying the alternating electric currents producing the rotating stator magnetic field that drives the rotor. The slots are numbered 1,2,...,12 circumferentially, starting from $\theta = 0$. The unstructured mesh is also displayed in Figure 9a and consists of 88,244 elements with 44,863 nodes and 134,589 d.o.f. Contrary to the idealized stator problem in Section 5.1, no symmetry conditions can be used here, requiring the discretization and modeling of the entire airgap and stator domains. The values of the geometric parameters of the stator are given in Table 9b.

Materials We use the material parameters of Table 4a. The corresponding magnetization curve is displayed in Figure 4b. As explained in subsection 4.3, for the case of the tightly packed conductors (case ii), the copper domain's magnetic energy density $W_{mag} = 0$ ($\chi = 0$) while its mechanical energy density W_{mech} is given by (4.5) with $G = 44\times10^9$Pa and $\nu = 0.33$.

Loading The stator is supplied by a three-phase alternating current of amplitude J_0 and cyclic frequency ω. We denote the phases A, B and C and we have the phase current densities $\boldsymbol{J}_A, \boldsymbol{J}_B$ and $\boldsymbol{J}_C$. The distributed 4 pole stator wiring adopted here is detailed in Figure 9a where the conductors $\mathscr{C}_{1,2,\dots,12}$ are

[17] $\mathscr{D}_1$ is reserved to the rotor domain (not shown in Figure 9a).

given the following current densities

$$\mathscr{C}_1 \cup \mathscr{C}_{10} : \quad \boldsymbol{J} = \boldsymbol{J}_A \; ; \quad \mathscr{C}_4 \cup \mathscr{C}_7 : \quad \boldsymbol{J} = -\boldsymbol{J}_A \; ; \quad \boldsymbol{J}_A = J_0 \cos(\omega t)\boldsymbol{e}_z \; ,$$

$$\mathscr{C}_2 \cup \mathscr{C}_{11} : \quad \boldsymbol{J} = \boldsymbol{J}_B \; ; \quad \mathscr{C}_5 \cup \mathscr{C}_8 : \quad \boldsymbol{J} = -\boldsymbol{J}_B \; ; \quad \boldsymbol{J}_B = J_0 \cos(\omega t + \frac{2\pi}{3})\boldsymbol{e}_z \; , \tag{5.6}$$

$$\mathscr{C}_3 \cup \mathscr{C}_{12} : \quad \boldsymbol{J} = \boldsymbol{J}_C \; ; \quad \mathscr{C}_6 \cup \mathscr{C}_9 : \quad \boldsymbol{J} = -\boldsymbol{J}_C \; ; \quad \boldsymbol{J}_C = J_0 \cos(\omega t + \frac{4\pi}{3})\boldsymbol{e}_z \; .$$

Simulations are performed with an input current amplitude $J_0 = 36\% m_s/R_2 \approx 10^7 A/m^2$; this value is chosen so that the numerically calculated magnetization nowhere exceeds its saturation value, thus operating within the range of the fitted magnetic response, as shown in Figure 4b. The current density is constant within the corresponding blue, light gray and red domains depicted in Figure 9a.

Magnetic boundary conditions We assume the plain ferromagnetic rotor $\mathscr{D}_1$ has infinite permeability, i.e. $\mathscr{D}_1 : \; \boldsymbol{H} = \boldsymbol{0}$, which matches the natural (Neumann) boundary condition $\partial\mathscr{D}_1 : \; \boldsymbol{N} \times \boldsymbol{H} = \boldsymbol{0}$. On the outer stator boundary, we assume negligible leakage flux, as for the idealized stator case (see (5.2))

$$\partial\mathscr{D}_3 : \qquad A = 0 \; , \tag{5.7}$$

implying that the radial component of the magnetic field vanishes ($\partial A/\partial\theta = B_r = \boldsymbol{N}\cdot\boldsymbol{B} = 0$).

Mechanical boundary conditions Similarly to the idealized rotor case (see (5.3)), the displacements are constrained to zero on the inner airgap boundary $\partial\mathscr{D}_1$[18].

$$\partial\mathscr{D}_1 : \qquad u_r = u_\theta = 0 \; . \tag{5.8}$$

Similarly to the idealized stator case in subsection 5.1, no constraints are imposed on the outer stator boundary and hence the corresponding natural (Neumann) boundary conditions are on $\partial\mathscr{D}_3 : \sigma_{rr} \approx \Pi_{rr} = 0, \sigma_{r\theta} \approx \Pi_{r\theta} = 0$.

Normalization In order to present results in dimensionless form, the same normalization (5.5) as for the cylindrical rotor is adopted.

The results of the FEM calculations for the magnetic constitutive law of (4.6) and the corresponding material parameters in Table 4a are presented in Figures 10 to 12 for the loosely packed conductors (case i) and in Figures 13 to 14 for the tightly packed conductors (case ii).

[18] Recall that the airgap has a very small stiffness, as discussed in subsection 4.2.

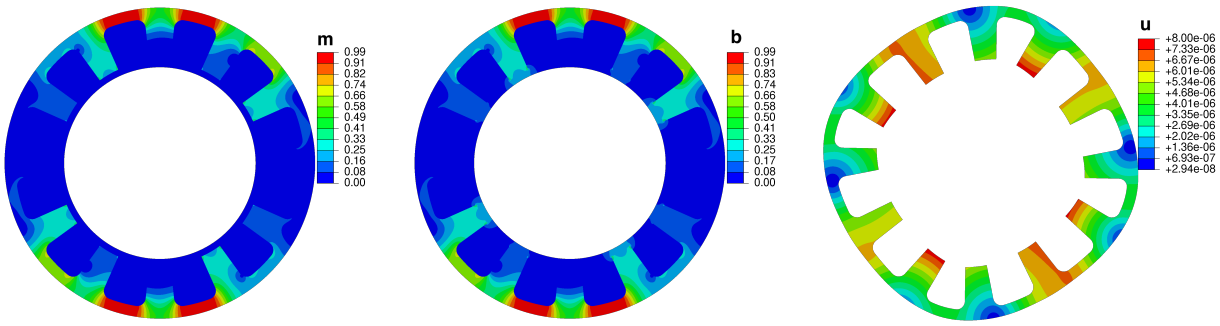

(a) $\|\boldsymbol{m}\|/m_s$ (b) $\|\boldsymbol{b}\|/\mu_0 m_s$ (c) $\|\boldsymbol{u}\|/R_2$

Figure 10: FEM results for the realistic stator with loosely packed conductors (case i). Contours in (a) dimensionless magnetization $\|\boldsymbol{m}\|/m_s$, in (b) dimensionless magnetic field $\|\boldsymbol{b}\|/\mu_0 m_s$ and in (c) dimensionless displacement $\|\boldsymbol{u}\|/R_2$. The displacement norm contours are plotted over an exaggerated deformed configuration (magnification factor: 10^4).

More specifically, the results of the numerical calculations for the realistic stator with loosely packed conductors (case i) depict the contours of the dimensionless magnetization $\|\boldsymbol{m}\|/m_s$ in Figure 10a, the contours of the dimensionless magnetic field $\|\boldsymbol{b}\|/\mu_0 m_s$ in Figure 10b and the contours of the dimensionless displacement $\|\boldsymbol{u}\|/R_2$ in Figure 15a. The latter are plotted over an exaggerated deformed configuration (magnification factor: 10^4). By comparing Figures 10a and 10b one notices that magnetic saturation is reached at the top and bottom parts of the stator and that the corresponding contours are practically identical, due to magnetic saturation. The (exaggerated) deformed configuration is depicted in Figure 15a and reflects the symmetry of the stator and the applied loading, as seen in Figure 9a. As expected the maximum deformation remains negligible and is of the order of 10^{-6}m. Notice that the thinner, cylindrical outer part of the stator deforms more than its thicker teeth.

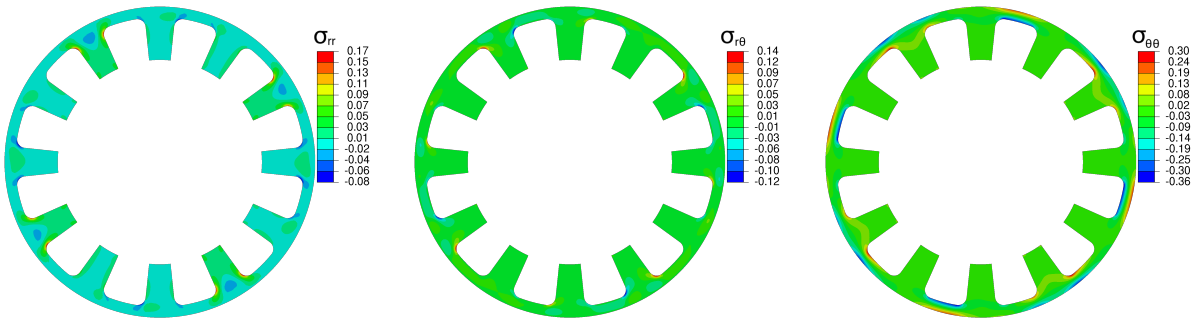

(a) $\sigma_{rr}/\mu_0 m_s^2$ (b) $\sigma_{r\theta}/\mu_0 m_s^2$ (c) $\sigma_{\theta\theta}/\mu_0 m_s^2$

Figure 11: FEM results for the realistic stator with loosely packed conductors (case i) at large values magnetic field $\|\boldsymbol{b}\|$. Contours in (a) dimensionless total radial stress $\sigma_{rr}/\mu_0 m_s^2$ vs r, in (b) dimensionless total tangential stress $\sigma_{r\theta}/\mu_0 m_s^2$ vs r and in (c) dimensionless total hoop stress $\sigma_{\theta\theta}/\mu_0 m_s^2$ vs r.

Next come the total stress results of the numerical calculations for the realistic stator with loosely packed conductors (case i). Contours of the dimensionless radial stress $\sigma_{rr}/\mu_0 m_s^2$ are shown in Figure 11a, for the dimensionless shear stress $\sigma_{r\theta}/\mu_0 m_s^2$ in Figure 11b and for the dimensionless hoop stress $\sigma_{\theta\theta}/\mu_0 m_s^2$ in Figure 11c. Stresses are maximized at the cylindrical part of the stator and at the base of the teeth where the magnetic field is maximized.

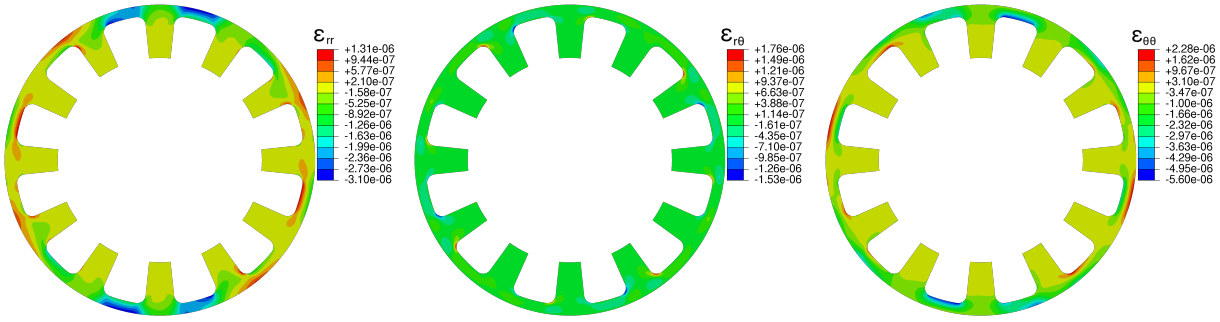

(a) ϵ_{rr} (b) $\epsilon_{r\theta}$ (c) $\epsilon_{\theta\theta}$

Figure 12: FEM results for the realistic stator with loosely packed conductors (case i) at large values magnetic field $\|\boldsymbol{b}\|$. Contours in (a) radial strain ϵ_{rr} vs r, in (b) shear strain $\epsilon_{r\theta}$ vs r and in (c) hoop strain $\epsilon_{\theta\theta}$ vs r.

Finally come the strain results of the numerical calculations for the realistic stator with loosely packed conductors (case i). Contours of the dimensionless radial strain ϵ_{rr} are shown in Figure 12a, for the dimensionless shear strain $\epsilon_{r\theta}$ in Figure 12b and for the dimensionless hoop strain $\epsilon_{\theta\theta}$ in Figure 12c. Strains are maximized at the cylindrical part of the stator and at the base of the teeth where the magnetic field is maximized. Notice however that even at their highest values they never exceed 10^{-5}, thus establishing that the stator's mechanical response is well within its linear elastic regime.

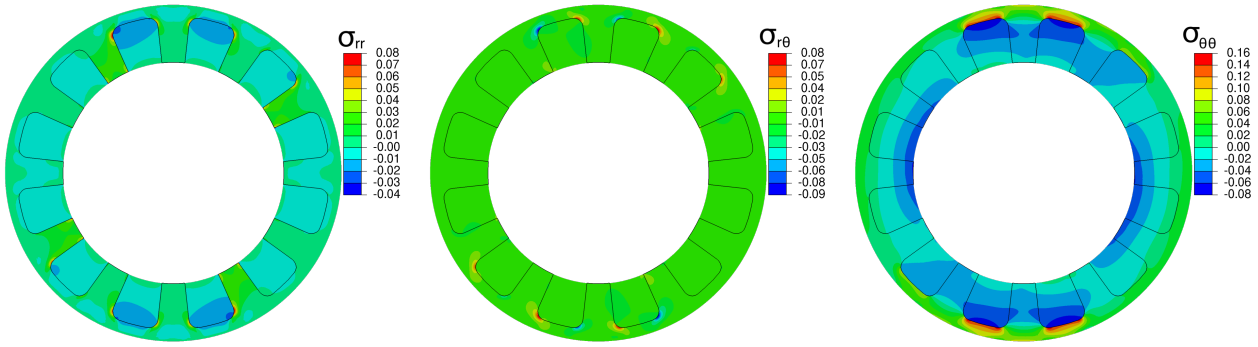

(a) $\sigma_{rr}/\mu_0 m_s^2$ (b) $\sigma_{r\theta}/\mu_0 m_s^2$ (c) $\sigma_{\theta\theta}/\mu_0 m_s^2$

Figure 13: FEM results for the realistic stator with tightly packed conductors (case ii) at large values magnetic field $\|\boldsymbol{b}\|$. Contours in (a) dimensionless total radial stress $\sigma_{rr}/\mu_0 m_s^2$ vs r, in (b) dimensionless total tangential stress $\sigma_{r\theta}/\mu_0 m_s^2$ vs r and in (c) dimensionless total hoop stress $\sigma_{\theta\theta}/\mu_0 m_s^2$ vs r.

Results of the numerical calculations for the realistic stator with tightly packed conductors (case ii) are presented next, starting with the components of the total stress field in Figure 13. For its mechanical response the stator appears as a bimetallic cylinder (gaps between teeth filled with copper and bonded to steel) thus significantly stiffening it compared to case (i). Contours of the dimensionless radial stress $\sigma_{rr}/\mu_0 m_s^2$ are shown in Figure 13a, for the dimensionless shear stress $\sigma_{r\theta}/\mu_0 m_s^2$ in Figure 13b and for the dimensionless hoop stress $\sigma_{\theta\theta}/\mu_0 m_s^2$ in Figure 13c. Stresses are maximized at the cylindrical part of the stator and at the base of the teeth where the magnetic field is maximized. As a result, maximum stresses reached for the tightly packed conductors in Figure 13 are significantly lower with respect to the corresponding stresses in the loosely packed case in Figure 11.

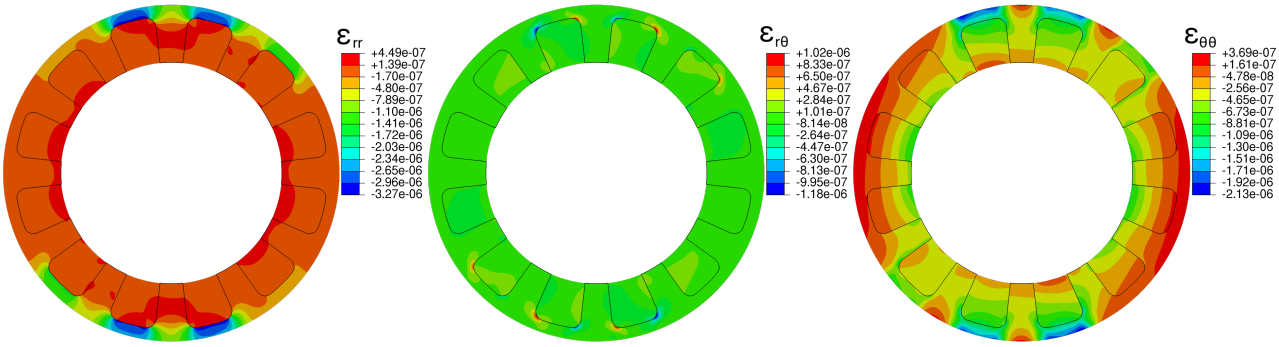

(a) ϵ_{rr} (b) $\epsilon_{r\theta}$ (c) $\epsilon_{\theta\theta}$

Figure 14: FEM results for the realistic stator with tightly packed conductors (case ii) at large values magnetic field $\|\boldsymbol{b}\|$. Contours in (a) radial strain ϵ_{rr} vs r, in (b) shear strain $\epsilon_{r\theta}$ vs r and in (c) hoop strain $\epsilon_{\theta\theta}$ vs r.

Lastly come the strain results of the numerical calculations for the realistic stator with tightly packed conductors (case ii) with the components of the strain field presented in Figure 14. Contours of the dimensionless radial strain ϵ_{rr} are shown in Figure 14a, for the dimensionless shear strain $\epsilon_{r\theta}$ in Figure 14b and for the dimensionless hoop strain $\epsilon_{\theta\theta}$ in Figure 14c. Strains are maximized at the cylindrical part of the stator and at the base of the teeth where the magnetic field is maximized. As a result of the stiffening response of the coils, maximum strains reached for the tightly packed conductors in Figure 14 are lower with respect to the corresponding strains in the loosely packed case in Figure 12.

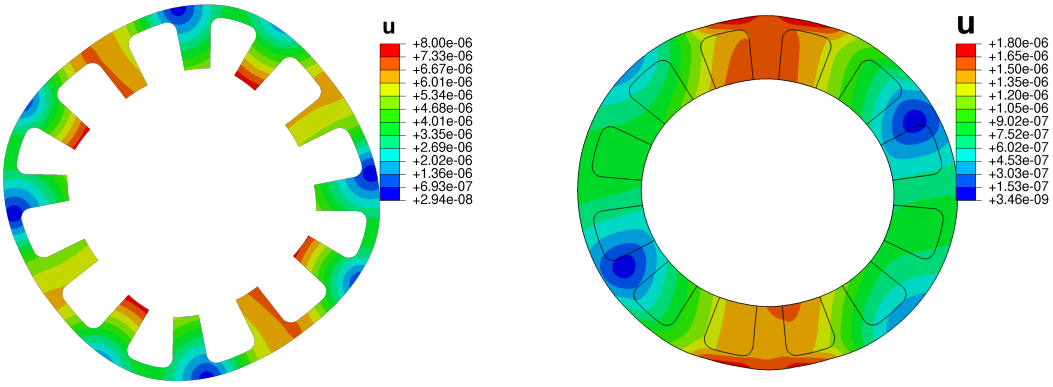

(a) $\|\boldsymbol{u}\|/R_2$ (b) $\|\boldsymbol{u}\|/R_2$

Figure 15: Deformed configuration ($\times 10,000$) of the loosely packed coils in (a) and the tightly packed ones ($\times 50,000$) in (b). Notice the considerably smaller distortion in (b) in spite of the five times larger magnification than (a).

Finally a comparison between the (exaggerated) deformed configurations of the stator in cases (i) and (ii) are presented in Figure 15, showing not only an almost lower order of magnitude displacements in the stiffer case (ii) but a different overall deformation pattern than the softer stator of case (i) as well, as observed by comparing Figure 15a to Figure 15b.

6. Conclusion

The increasing importance of environmental constraints in the transportation industry requires novel electric motor designs to meet technological challenges of cost, weight and efficiency. Modeling of electric motors has in the past been predominantly focussed on calculating magnetic fields and torque. Given the increased rotation speeds, currents and electromagnetic field levels, mechanical field (stress and strain) calculations are gaining importance for producing optimized motor designs. To this end, the authors proposed in Hanappier et al. (2021a) a thermodynamicaly consistent framework – based on the direct (current configuration) approach of continuum mechanics – for the concurrent calculation of mechanical and electromagnetic fields in electric motors, accompanied by analytical examples of idealized electric motor problems Hanappier et al. (2021a,b).

Due to the complex geometry of a typical electric motor, numerical solutions of the coupled magneto-mechanical governing equations are required. To this end, a Lagrangian (reference configuration) variational principle is proposed for the eddy current approximation that properly retrieves the Maxwell stresses and is consistent with its direct approach counterpart. An FEM discretization method based on this variational principle is subsequently proposed for the simultaneous solution of the magnetic (Maxwell-Ampère's) and mechanical (Newton's) governing equations. The method is first applied to a cylindrical stator, where an analytical solution can be found for the linear elastic and magnetization regimes, thus providing firstly

an independent code verification and subsequently an assessment of the influence of the stator's nonlinear magnetic response. The approach is subsequently used to tackle a realistic geometry stator with two pole pairs under a three-phase current for two different cases: loosely or tightly packed conducting wires to calculate the corresponding magnetic and stress fields. The results of our calculations show the influence of magnetic saturation effects as well of the current conducting coils on the stress, strain and magnetic fields.

The novelty – and advantage of the proposed variational approach – lies first in the concurrent solution of the magnetic and mechanical governing equations without the need of stepwise methods and then in the simplicity of the FEM discretization scheme since no special elements are needed, just considering magnetic potential and displacement variables as the nodal d.o.f. Although the application presented pertains to a stator, the proposed methodology can be generalized to the calculation of a complete motor with rotating parts and a more complicated, coupled magneto-mechanical constitutive response.

ACKNOWLEDGMENTS

The work of N. Hanappier is supported by a Fellowship from the *André Citroën Chair* of the Ecole Polytechnique. The paper at hand is dedicated to Prof. J. R. Barber's in honor of his 80th birthday. In addition, N. Triantafyllidis wants to express his gratitude to an excellent colleague for thirty years and loyal friend since 1981 for his wisdom and advice over the years. The recently introduced by the authors Hanappier et al. (2021a) small strain, arbitrary magnetization formulation in magnetoelasticity and used in this work is the belated answer to questions discussed with Prof. Barber several years ago but only recently answered, thus motivating the contribution of this paper to the special issue of the *I.J.S.S.* dedicated to an excellent scholar in solid mechanics and rare role model.

7. References

References

Abdel-Razek, A., Coulomb, J., Feliachi, M., Sabonnadiere, J., 1982. Conception of an air-gap element for the dynamic analysis of the electromagnetic field in electric machines. IEEE Transactions on Magnetics 18, 655–659. URL: https://ieeexplore.ieee.org/abstract/document/1061898.

Arkkio, A., 1987. Analysis of induction motors based on the numerical solution of the magnetic field and circuit equations , 97URL: http://urn.fi/urn:nbn:fi:tkk-001267.

Boules, N., 1984. Two-dimensional field analysis of cylindrical machines with permanent magnet excitation. IEEE Transactions on Industry Applications IA-20, 1267–1277.

Chari, M.V.K., Silvester, P., 1971. Analysis of turboalternator magnetic fields by finite elements. IEEE Transactions on Power Apparatus and Systems PAS-90, 454–464. URL: https://ieeexplore.ieee.org/abstract/document/4074358.

Danas, K., 2017. Effective response of classical, auxetic and chiral magnetoelastic materials by use of a new variational principle. Journal of the Mechanics and Physics of Solids 105, 25 – 53.

Daniel, L., Bernard, L., Hubert, O., 2020. Multiscale Modeling of Magnetic Materials. Elsevier.

Devillers, E., Hecquet, M., Cimetiere, X., Lecointe, J.P., Le Besnerais, J., Lubin, T., 2018a. Experimental benchmark for magnetic noise and vibrations analysis in electrical machines, in: 2018 XIII International Conference on Electrical Machines (ICEM), IEEE. pp. 745–751. doi:10.1109/ICELMACH.2018.8506928.

Devillers, E., Le Besnerais, J., Lubin, T., Hecquet, M., Lecointe, J., 2016. A review of subdomain modeling techniques in electrical machines: Performances and applications, in: 2016 XXII International Conference on Electrical Machines (ICEM), pp. 86–92. URL: https://ieeexplore.ieee.org/abstract/document/7732510.

Devillers, E., Le Besnerais, J., Lubin, T., Hecquet, M., Lecointe, J.P., 2018b. An improved 2D subdomain model of squirrel cage induction machine including winding and slotting harmonics at steady state. IEEE Transactions on Magnetics URL: https://hal.archives-ouvertes.fr/hal-01679361, doi:10.1109/TMAG.2017.2782222.

Fonteyn, K., Belahcen, A., Kouhia, R., Rasilo, P., Arkkio, A., 2010a. Fem for directly coupled magneto-mechanical phenomena in electrical machines. IEEE Transactions on Magnetics 46, 2923–2926.

Fonteyn, K.A., Belahcen, A., Rasilo, P., Kouhia, R., Arkkio, A., 2010b. Contribution of maxwell stress in air on the deformations of induction machines, in: 2010 International Conference on Electrical Machines and Systems, pp. 1749–1753.

Hanappier, N., 2021. Coupled Electro-Magneto-Thermo-Mechanical Modeling of Electric Motors. Ph.D. thesis. Ecole Polytechnique.

Hanappier, N., Charkaluk, E., Triantafyllidis, N., 2021a. A coupled electromagnetic–thermomechanical approach for the modeling of electric motors. Journal of the Mechanics and Physics of Solids 149, 104315.

Hanappier, N., Charkaluk, E., Triantafyllidis, N., 2021b. Multiphysics simulation of electric motors – analytical solution for stators. submitted to IEEE Magnetic Transactions .

Huppunen, J., et al., 2004. High-speed solid-rotor induction machine–electromagnetic calculation and design URL: https://lutpub.lut.fi/handle/10024/36551.

Javadi, H., Lefèvre, Y., Clénet, S., Mazenc, M., 1995. Electro-magneto-mechanical characterizations of the vibration of magnetic origin of electrical machines. IEEE transactions on magnetics 31, 1892–1895. URL: https://ieeexplore.ieee.org/abstract/document/376408.

Kovetz, A., 2000. Electromagnetic theory. volume 975. Oxford University Press Oxford.

López, I., Ibarra, E., Matallana, A., Andreu, J., Kortabarria, I., 2019. Next generation electric drives for hev/ev propulsion systems: Technology, trends and challenges. Renewable and Sustainable Energy Reviews 114, 109336. URL: http://www.sciencedirect.com/science/article/pii/S1364032119305441, doi:https://doi.org/10.1016/j.rser.2019.109336.

Lubin, T., Mezani, S., Rezzoug, A., 2011. Analytic calculation of eddy currents in the slots of electrical machines: Application to cage rotor induction motors. IEEE Transactions on Magnetics 47, 4650–4659. doi:10.1109/TMAG.2011.2157167.

Rekik, M., Hubert, O., Daniel, L., 2014. Influence of a multiaxial stress on the reversible and irreversible magnetic behaviour of a 3% si-fe alloy. International Journal of Applied Electromagnetics and Mechanics 44, 301–315.

Reyne, G., Sabonnadiere, J.C., Imhoff, J.F., 1988. Finite element modelling of electromagnetic force densities in dc machines. IEEE Transactions on Magnetics 24, 3171–3173. URL: https://ieeexplore.ieee.org/abstract/document/92371.

Silvester, P., Cabayan, H.S., Browne, B.T., 1973. Efficient techniques for finite element analysis of electric machines. IEEE Transactions on Power Apparatus and Systems PAS-92, 1274–1281. URL: https://ieeexplore.ieee.org/abstract/document/4075205.

Thomas, J., Triantafyllidis, N., 2009. On electromagnetic forming processes in finitely strained solids: Theory and examples. Journal of the Mechanics and Physics of Solids 57, 1391 – 1416. URL: http://www.sciencedirect.com/science/article/pii/S0022509609000465, doi:https://doi.org/10.1016/j.jmps.2009.04.004.

Vandevelde, L., Gyselinck, J., Wulf, M.D., Melkebeek, J., 2004. Finite-element computation of the deformation of ferromagnetic material taking into account magnetic forces and magnetostriction. IEEE Transactions on Magnetics 40, 565 – 568.

Zhu, Z.Q., Howe, D., Bolte, E., Ackermann, B., 1993. Instantaneous magnetic field distribution in brushless permanent

magnet dc motors. i. open-circuit field. IEEE Transactions on Magnetics 29, 124–135. URL: https://ieeexplore.ieee.org/abstract/document/195557/references#references.

Appendix A. Analytical solution of cylindrical stator

The analytical solution for the idealized (cylindrical) motor problem – stator, airgap and rotor – is presented in detail (and in the more general setting of $\Lambda \neq 0$) in Hanappier et al. (2021b). A brief summary of the results for the stator are given here for completeness of the presentation, obtained in the linear small strain, small magnetization regime and hence expressed in the current configuration, i.e. $\boldsymbol{A} \approx \boldsymbol{a}$, $\boldsymbol{B} \approx \boldsymbol{b}$, $\boldsymbol{H} \approx \boldsymbol{h}$, $\boldsymbol{\Pi} \approx \boldsymbol{\sigma}$.

The equations to be solved are respectively: Maxwell-Ampère (no distributed currents) in the airgap and the stator[19]

$$\boldsymbol{x} \in \mathscr{D}_2 \cup \mathscr{D}_3 : \quad \boldsymbol{\nabla}^2 a = 0 \; ; \; \boldsymbol{b} = \boldsymbol{\nabla} \times \boldsymbol{a} = \frac{1}{r}\frac{\partial a}{\partial \theta}\boldsymbol{e}_r - \frac{\partial a}{\partial r}\boldsymbol{e}_\theta \; , \tag{A.1}$$

and the linear momentum balance in the stator[20]:

$$\boldsymbol{x} \in \mathscr{D}_3 : \quad \boldsymbol{\nabla} \cdot \boldsymbol{\sigma} = 0 \; ; \; \boldsymbol{\sigma} = \overset{e}{\boldsymbol{\sigma}} + \overset{m}{\boldsymbol{\sigma}} \; ; \; \overset{e}{\boldsymbol{\sigma}} \equiv 2G[\boldsymbol{\epsilon} + \frac{\nu}{1-2\nu}\mathrm{tr}(\boldsymbol{\epsilon})\boldsymbol{I}] \; , \; \overset{m}{\boldsymbol{\sigma}} \equiv \frac{1}{\mu_0(1+\chi)}\left[\boldsymbol{b}\boldsymbol{b} - \frac{1-\chi}{2}(\boldsymbol{b}\cdot\boldsymbol{b})\boldsymbol{I}\right] \; . \tag{A.2}$$

It should be added here that for the airgap domain, the equilibrium equation becomes $\boldsymbol{\nabla} \cdot \overset{m}{\boldsymbol{\sigma}} = 0$ where the magnetic stress $\overset{m}{\boldsymbol{\sigma}}$ is the Maxwell stress of the vacuum $\boldsymbol{\sigma}_{Maxw} = \boldsymbol{b}\boldsymbol{b} - 0.5(\boldsymbol{b}\cdot\boldsymbol{b})$ (for the air $\chi = 0$).

The following dimensionless variables and parameters are introduced in Hanappier et al. (2021b)

$$\frac{r}{R_2} \to r \; , \quad r_1 \equiv \frac{R_1}{R_2} \; , \quad r_3 \equiv \frac{R_3}{R_2} \; , \quad \frac{a}{\frac{R_1 B_0}{p}} \to a \; , \quad \frac{\boldsymbol{u}}{\frac{p^2 a_0^2}{2\mu_0 R_2 G}} \to \boldsymbol{u} \; , \quad \frac{\boldsymbol{\sigma}}{\frac{p^2 a_0^2}{2\mu_0 R_2 G}} \to \boldsymbol{\sigma} \; , \tag{A.3}$$

with the dimensionless variables and field quantities of the problem, r, a, $\boldsymbol{u}$, $\boldsymbol{\sigma}$ henceforth denoted by the same symbol as their dimensioned counterparts.

The solution for the dimensionless magnetic potential $\boldsymbol{a}$ is,

$$\begin{gathered}
\boldsymbol{x} \in \mathscr{D}_2 : \quad a_2(r,\theta,t) = A_2(r)\cos\Theta \; ; \quad A_2(r) \equiv (Dr^p + Er^{-p}) \; , \quad \Theta \equiv p\theta - \omega t \; , \\
\\
\boldsymbol{x} \in \mathscr{D}_3 : \quad a_3(r,\theta,t) = A_3(r)\cos\Theta \; ; \quad A_3(r) \equiv (Fr^p + Gr^{-p}) \; , \\
\\
D \equiv \frac{\left[\chi r_3^p - (2+\chi) r_3^{-p}\right]}{\chi(r_3^p - r_3^{-p})(r_1^p + r_1^{-p}) + 2(r_3^p r_1^{-p} - r_3^{-p} r_1^p)} \; , \; E \equiv \frac{\left[(2+\chi) r_3^p - \chi r_3^{-p}\right]}{\chi(r_3^p - r_3^{-p})(r_1^p + r_1^{-p}) + 2(r_3^p r_1^{-p} - r_3^{-p} r_1^p)} \; , \\
\\
F \equiv \frac{-2(1+\chi) r_3^{-p}}{\chi(r_3^p - r_3^{-p})(r_1^p + r_1^{-p}) + 2(r_3^p r_1^{-p} - r_3^{-p} r_1^p)} \; , \; G \equiv \frac{2(1+\chi) r_3^p}{\chi(r_3^p - r_3^{-p})(r_1^p + r_1^{-p}) + 2(r_3^p r_1^{-p} - r_3^{-p} r_1^p)} \; ,
\end{gathered} \tag{A.4}$$

[19] Boundary conditions are discussed in subsection 5.1.

[20] See footnote 19

and the components of the magnetic field can be calculated with the help of $(A.1)_2$.

At the stator $\mathscr{D}_3$, the components of the elastic stress field $\overset{e}{\boldsymbol{\sigma}}$ in $(A.2)_3$ are obtained in terms the Airy stress function ϕ

$$\overset{e}{\sigma}_{rr} = \frac{1}{r}\frac{\partial \phi}{\partial r} + \frac{1}{r^2}\frac{\partial^2 \phi}{\partial \theta^2} + V \ , \quad \overset{e}{\sigma}_{\theta\theta} = \frac{\partial^2 \phi}{\partial r^2} + V \ , \quad \overset{e}{\sigma}_{r\theta} = -\frac{\partial}{\partial r}\left(\frac{1}{r}\frac{\partial \phi}{\partial \theta}\right) \ . \tag{A.5}$$

The Airy stress function ϕ consists of a homogeneous part ϕ_h and a particular part ϕ_V

$$\phi = \phi_h + \phi_V \ ,$$

$$\begin{aligned} \phi_h(r,\theta,t) = {} & \Phi_{01} r^2 + \Phi_{02} r^2 \ln(r) + \Phi_{03} \ln(r) + \Phi_{04}\theta \\ & + \left(\Phi_{c1} r^{-2p+2} + \Phi_{c2} r^{2p} + \Phi_{c3} r^{-2p} + \Phi_{c4} r^{2p+2}\right) \cos(2\Theta) \\ & + \left(\Phi_{s1} r^{-2p+2} + \Phi_{s2} r^{2p} + \Phi_{s3} r^{-2p} + \Phi_{s4} r^{2p+2}\right) \sin(2\Theta) \ , \end{aligned} \tag{A.6}$$

$$\phi_V(r,\theta,t) = -\frac{1-2\nu}{1-\nu}\left(\int_0^r \frac{1}{r}\int_0^r V_0 r \mathrm{d}r \ \mathrm{d}r + \left[\frac{r^{2p}}{4p}\int_0^r V_c r^{-2p+1}\mathrm{d}r - \frac{r^{-2p}}{4p}\int_0^r V_c r^{2p+1}\mathrm{d}r\right]\cos(2\Theta)\right) .$$

$$V_0(r) = -\frac{s_m}{2p^2}\left[\frac{p^2}{r^2}A_3^2 + \left(\frac{dA_3}{dr}\right)^2\right] \ , \quad V_c(r) = -\frac{s_m}{2p^2}\left[-\frac{p^2}{r^2}A_3^2 + \left(\frac{dA_3}{dr}\right)^2\right] \ ; \quad s_m = \frac{1}{2}\frac{\chi}{1+\chi} \ .$$

The constants $\Phi_{01}, \Phi_{02}, \Phi_{03}, \Phi_{04}, \Phi_{c1}, \Phi_{c2}, \Phi_{c3}, \Phi_{c4}, \Phi_{s1}, \Phi_{s2}, \Phi_{s3}, \Phi_{s4}$ are evaluated numerically by application of the boundary condition for stress on $\partial\mathscr{D}_2$ and $\partial\mathscr{D}_3$.

Strains $\boldsymbol{\epsilon}$ are obtained by inverting the constitutive law in $(A.2)_3$ and the displacement field follows from the classical kinematic (strain-displacement) relationship of linear elasticity in polar coordinates.

Appendix B. Element force vector and stiffness matrix

For meshing flexibility purposes, the simplest FEM discretization method is used here, based on constant strain triangular 2D elements (one integration point at the element centroid) as depicted in Figure B.1. The corresponding degrees of freedom for the element $[\boldsymbol{q}_e]$ are[21]

$$[\boldsymbol{q}_e] = \{\ u_1^{(1)},\ u_2^{(1)},\ A^{(1)},\ u_1^{(2)},\ u_2^{(2)},\ A^{(2)},\ u_1^{(3)},\ u_2^{(3)},\ A^{(3)}\ \}^T \ , \tag{B.1}$$

where indices $(1), (2), (3)$ refer to the nodes of the element as depicted in Figure B.1.

[21] Standard matrix algebra notation is used here where vectors and matrices are denoted by bold symbols in brackets.

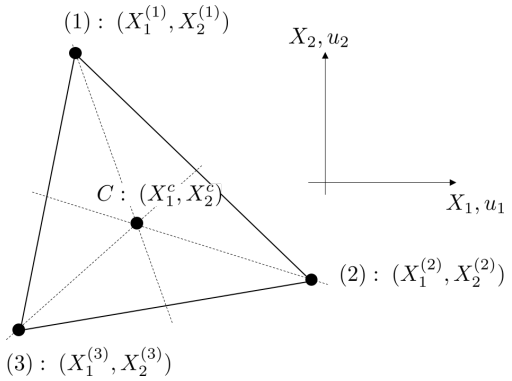

Figure B.1: Constant strain triangular elements used for the FEM discretization.

The vector of unknown fields $[\boldsymbol{q}(\boldsymbol{X})]$ in an element are found in terms of the nodal variables $\boldsymbol{q}_e$ and the shape functions $N_i(\boldsymbol{X}),\ 1 \leq i \leq 3$, where $\boldsymbol{X} = (X_1, X_2)$

$$[\boldsymbol{q}(\boldsymbol{X})] = \{u_1(\boldsymbol{X}), u_2(\boldsymbol{X}), A(\boldsymbol{X})\}^T = [\boldsymbol{N}(\boldsymbol{X})][\boldsymbol{q}_e]\ , \tag{B.2}$$

where the shape function matrix $[\boldsymbol{N}(\boldsymbol{X})]$ is given by

$$[\boldsymbol{N}(\boldsymbol{X})] = \begin{bmatrix} N_1(\boldsymbol{X}) & 0 & 0 & N_2(\boldsymbol{X}) & 0 & 0 & N_3(\boldsymbol{X}) & 0 & 0 \\ 0 & N_1(\boldsymbol{X}) & 0 & 0 & N_2(\boldsymbol{X}) & 0 & 0 & N_3(\boldsymbol{X}) & 0 \\ 0 & 0 & N_1(\boldsymbol{X}) & 0 & 0 & N_2(\boldsymbol{X}) & 0 & 0 & N_3(\boldsymbol{X}) \end{bmatrix}\ , \tag{B.3}$$

$$N_1(X_1, X_2) = \frac{1}{2A_e}\left[X_1^{(2)}X_2^{(3)} - X_1^{(3)}X_2^{(2)} + (X_2^{(2)} - X_2^{(3)})X_1 - (X_1^{(2)} - X_1^{(3)})X_2\right]\ ,$$

$$N_2(X_1, X_2) = \frac{1}{2A_e}\left[X_1^{(3)}X_2^{(1)} - X_1^{(1)}X_2^{(3)} + (X_2^{(3)} - X_2^{(1)})X_1 - (X_1^{(3)} - X_1^{(1)})X_2\right]\ ,$$

$$N_3(X_1, X_2) = \frac{1}{2A_e}\left[X_1^{(1)}X_2^{(2)} - X_1^{(2)}X_2^{(1)} + (X_2^{(1)} - X_2^{(2)})X_1 - (X_1^{(1)} - X_1^{(2)})X_2\right]\ ,$$

where A_e is the surface of the element.

The load vector for the element $[\boldsymbol{f}_e]$ is obtained by the first variation of the potential energy $\mathscr{P}$ in (4.1)

$$[\boldsymbol{f}_e]^T[\delta\boldsymbol{q}_e] = \int_{A_e}\left[\frac{\partial \mathscr{p}}{\partial F_{\alpha\beta}}\delta F_{\alpha\beta} + \frac{\partial \mathscr{p}}{\partial B_\epsilon}\delta B_\epsilon - \mathscr{f}\delta A\right]\mathrm{d}A_e\ , \tag{B.4}$$

where $\mathscr{p}$ is the system's energy density. The element stiffness matrix $[\boldsymbol{k}_e]$ is similarly obtained from the

second variation of the potential energy $\mathscr{P}$ in (4.1)

$$[\Delta \boldsymbol{q}_e]^T[\boldsymbol{k}_e][\delta \boldsymbol{q}_e] = \int_{A_e} \left[\frac{\partial^2 \mathscr{p}}{\partial F_{\alpha\beta}\partial F_{\delta\gamma}} \delta F_{\alpha\beta} \Delta F_{\delta\gamma} + \frac{\partial^2 \mathscr{p}}{\partial B_\epsilon \partial F_{\delta\gamma}} \delta B_\epsilon \Delta F_{\delta\gamma} \right. \\ \left. + \frac{\partial^2 \mathscr{p}}{\partial F_{\alpha\beta}\partial B_\zeta} \delta F_{\alpha\beta} \Delta B_\zeta + \frac{\partial^2 \mathscr{p}}{\partial B_\epsilon \partial B_\zeta} \delta B_\epsilon \Delta B_\zeta \right] \mathrm{d}A_e \, . \tag{B.5}$$

The calculation of the integrals in (B.4) and (B.5) requires the auxiliary step of evaluating the potential field A (at the element centroid), its (constant) derivatives (components of the magnetic field $B_1 = -\partial A/\partial X_2$ and $B_2 = \partial A/\partial X_1$) and the (constant) derivatives of the displacement field $\boldsymbol{u}$

$$\left\{ \frac{\partial u_1}{\partial X_1}, \ \frac{\partial u_1}{\partial X_2}, \ \frac{\partial u_2}{\partial X_1}, \ \frac{\partial u_2}{\partial X_2}, \ A, \ B_1, \ B_2 \right\}^T = [\boldsymbol{G}][\boldsymbol{q}_e] \, ,$$

$$[\boldsymbol{G}] = \begin{bmatrix} \frac{\partial N_1}{\partial X_1} & 0 & 0 & \frac{\partial N_2}{\partial X_1} & 0 & 0 & \frac{\partial N_3}{\partial X_1} & 0 & 0 \\ \frac{\partial N_1}{\partial X_2} & 0 & 0 & \frac{\partial N_2}{\partial X_2} & 0 & 0 & \frac{\partial N_3}{\partial X_2} & 0 & 0 \\ 0 & \frac{\partial N_1}{\partial X_1} & 0 & 0 & \frac{\partial N_2}{\partial X_1} & 0 & 0 & \frac{\partial N_3}{\partial X_1} & 0 \\ 0 & \frac{\partial N_1}{\partial X_2} & 0 & 0 & \frac{\partial N_2}{\partial X_2} & 0 & 0 & \frac{\partial N_3}{\partial X_2} & 0 \\ 0 & 0 & N_1^c & 0 & 0 & N_2^c & 0 & 0 & N_3^c \\ 0 & 0 & \frac{\partial N_1}{\partial X_2} & 0 & 0 & \frac{\partial N_2}{\partial X_2} & 0 & 0 & \frac{\partial N_3}{\partial X_2} \\ 0 & 0 & -\frac{\partial N_1}{\partial X_1} & 0 & 0 & -\frac{\partial N_2}{\partial X_1} & 0 & 0 & -\frac{\partial N_3}{\partial X_1} \end{bmatrix} , \tag{B.6}$$

where by N_i^c we denote evaluation of the shape function at the centroid of the element.

The force vector $[\boldsymbol{f}_e]$ for the element is thus found from (B.4) in terms of the first derivatives vector $[\boldsymbol{f}^\star]$

$$[\boldsymbol{f}_e] = A_e[\boldsymbol{G}]^T[\boldsymbol{f}^\star] \, ; \quad [\boldsymbol{f}^\star] = \left\{ \frac{\partial \mathscr{p}}{\partial F_{11}}, \ \frac{\partial \mathscr{p}}{\partial F_{12}}, \ \frac{\partial \mathscr{p}}{\partial F_{21}}, \ \frac{\partial \mathscr{p}}{\partial F_{22}}, \ -\mathscr{J}, \ \frac{\partial \mathscr{p}}{\partial B_1}, \ \frac{\partial \mathscr{p}}{\partial B_2} \right\}^T \, . \tag{B.7}$$

The element stiffness matrix $[\boldsymbol{k}_e]$ is found from (B.4) in terms of the second derivatives matrix $[\boldsymbol{k}^\star]$

$$[\boldsymbol{k}_e] = A_e[\boldsymbol{G}]^T[\boldsymbol{k}^\star][\boldsymbol{G}] \; ;$$

$$[\boldsymbol{k}^\star] = \begin{bmatrix} \frac{\partial^2 \wp}{\partial F_{11}\partial F_{11}} & \frac{\partial^2 \wp}{\partial F_{11}\partial F_{12}} & \frac{\partial^2 \wp}{\partial F_{11}\partial F_{21}} & \frac{\partial^2 \wp}{\partial F_{11}\partial F_{22}} & 0 & \frac{\partial^2 \wp}{\partial F_{11}\partial B_1} & \frac{\partial^2 \wp}{\partial F_{11}\partial B_2} \\ \frac{\partial^2 \wp}{\partial F_{12}\partial F_{11}} & \frac{\partial^2 \wp}{\partial F_{12}\partial F_{12}} & \frac{\partial^2 \wp}{\partial F_{12}\partial F_{21}} & \frac{\partial^2 \wp}{\partial F_{12}\partial F_{22}} & 0 & \frac{\partial^2 \wp}{\partial F_{12}\partial B_1} & \frac{\partial^2 \wp}{\partial F_{12}\partial B_2} \\ \frac{\partial^2 \wp}{\partial F_{21}\partial F_{11}} & \frac{\partial^2 \wp}{\partial F_{21}\partial F_{12}} & \frac{\partial^2 \wp}{\partial F_{21}\partial F_{21}} & \frac{\partial^2 \wp}{\partial F_{21}\partial F_{22}} & 0 & \frac{\partial^2 \wp}{\partial F_{21}\partial B_1} & \frac{\partial^2 \wp}{\partial F_{21}\partial B_2} \\ \frac{\partial^2 \wp}{\partial F_{22}\partial F_{11}} & \frac{\partial^2 \wp}{\partial F_{22}\partial F_{12}} & \frac{\partial^2 \wp}{\partial F_{22}\partial F_{21}} & \frac{\partial^2 \wp}{\partial F_{22}\partial F_{22}} & 0 & \frac{\partial^2 \wp}{\partial F_{22}\partial B_1} & \frac{\partial^2 \wp}{\partial F_{22}\partial B_2} \\ 0 & 0 & 0 & 0 & 0 & 0 & 0 \\ \frac{\partial^2 \wp}{\partial B_1\partial F_{11}} & \frac{\partial^2 \wp}{\partial B_1\partial F_{12}} & \frac{\partial^2 \wp}{\partial B_1\partial F_{21}} & \frac{\partial^2 \wp}{\partial B_1\partial F_{22}} & 0 & \frac{\partial^2 \wp}{\partial B_1\partial B_1} & \frac{\partial^2 \wp}{\partial B_1\partial B_2} \\ \frac{\partial^2 \wp}{\partial B_2\partial F_{11}} & \frac{\partial^2 \wp}{\partial B_2\partial F_{12}} & \frac{\partial^2 \wp}{\partial B_2\partial F_{21}} & \frac{\partial^2 \wp}{\partial B_2\partial F_{22}} & 0 & \frac{\partial^2 \wp}{\partial B_2\partial B_1} & \frac{\partial^2 \wp}{\partial B_2\partial B_2} \end{bmatrix} \tag{B.8}$$

The numerical implementation is based on software *Abaqus* via a user element, which provides the element force vector $[\boldsymbol{f}_e]$ and the element stiffness matrix $[\boldsymbol{k}_e]$, given respectively by (B.7) and (B.8). Following the assembly of the global force vector and stiffness matrix from its element counterparts, the algorithm solves the resulting FEM-discretized nonlinear system using a Newton-Raphson algorithm.